Chinese Journal of Mechanical Engineering: Additive Manufacturing Frontiers 2 (2023) 100102

Contents lists available at ScienceDirect

Chinese Journal of Mechanical Engineering: Additive Manufacturing Frontiers

journal homepage: www.elsevier.com/locate/cjmeamf

A Review of Residual Stress and Deformation Modeling for Metal Additive Manufacturing Processes

Asim Rashid*, Aditya Gopaluni

Department of Mechanical and Materials Engineering, University of Turku, FI-20014, Finland

ARTICLE INFO

Keywords:
Modeling additive manufacturing
Residual stress in AM
Finite element analysis of AM process
Simulation of AM
Residual strain and deformation
Macro-scale model

ABSTRACT

A metal additive manufacturing process results in a nearly net-shaped fabrication of parts directly from digital data. A local heat source melts the deposited material, and a part is built layer-by-layer. Residual stress and deformation are critical issues experienced by additively manufactured parts. Modeling the additive manufacturing process provides important insights and can help determine an optimal build plan so as to minimize residual stress formation. Various approaches have been used for modeling of residual stresses, ranging from high-fidelity models to simplified models, for quicker results. This paper provides a state-of-the-art review of the approaches used to numerically model residual deformation and stresses in structures built using additive manufacturing. Furthermore, it describes the physical causes of residual-stress generation in an additively manufactured structure.

1. Introduction

Diverse additive manufacturing (AM) processes are used to build metal parts [1]. Although the processes vary widely in detail, the generic layer-by-layer process can be defined as a process in which a local heat source melts a small volume of previously deposited material (or substrate) and an additional volume of new material, while the heat source moves relative to the substrate and deposited material [2]. An AM process results in nearly net-shaped manufacturing of parts directly from computer-aided design (CAD) data. The main AM processes for metals include powder bed fusion (PBF) and directed energy deposition (DED). PBF includes all processes in which an energy source (electron beam or laser beam) is used to selectively melt or sinter a layer of a powder bed. After a layer is completely built, a new layer of powder is spread over the built area, and the energy source begins to scan. The DED method includes processes in which an energy source, such as a laser beam, electron beam, or plasma/electric arc, is used to fuse materials in the form of a powder or wire by directly melting them as they are being deposited [3,4].

AM processes allow the construction of geometrically complex components with very little material waste. AM enables the fabrication of optimized part geometries, for example, using topology optimization tools and lattice structures [5,6]. However, several challenges must be overcome to take full advantage of AM. One of the most critical challenges that impedes the adoption of AM processes is the formation of residual stresses and geometric distortion [7–10].

Residual stresses are defined as stresses that remain within a part of the environment after it reaches equilibrium [11]. In several manufacturing processes, permanent stresses develop in a component even after external causes, such as temperature gradients or forces, have been removed. In the case of the presence of thermal stresses in a part, if they are large enough to cause yielding, these stresses may develop into residual stresses after cooling [12,13]. Residual stress can cause distortion of an AM part after removal from the build platform, such that the part does not conform to the required geometric tolerances (see Fig. 1). Furthermore, residual stresses can cause cracking and are detrimental to fatigue resistance [14–20]. Although post-process heat treatments can be performed to alleviate residual stresses, they increase the production time and cost [21]. Furthermore, these stresses may cause parts to fail during construction.

Residual stresses are generally classified according to their length scales [23,24]. Type-I residual stresses are macroscopic stresses that vary over large distances. They affect the scale of the component geometry and can result in distortion of the part. Type II residual stresses act on the individual grain scales. These stresses are formed owing to the local microstructural effects. Type III residual stresses act on the atomic scale. Type I stresses cause distortion during and/or after part fabrication. These stresses can cause loss of geometric tolerance after they are removed from the build plate. Furthermore, they can affect the fatigue life of the built components. Therefore, they are of interest from the perspectives of product design and operation and will be the focus of this review.

* Corresponding author.
E-mail address: asim.rashid@utu.fi (A. Rashid).

https://doi.org/10.1016/j.cjmeam.2023.100102
Received 4 January 2023; Received in revised form 22 June 2023; Accepted 15 August 2023
Available online 29 October 2023

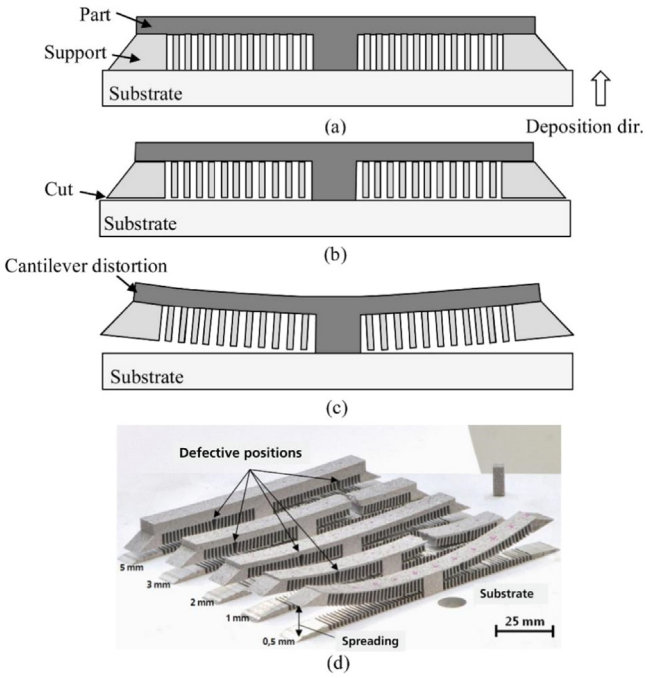

Fig. 1. Distortion in a twin cantilever beam due to residual stresses: (a) Building strategy; (b) Cutting of support from the substrate; (c) Distortion after support removal; (d) Macrograph of cantilever with different arm thicknesses after cutting of support [22].

1.1. Source of residual stresses

In Fig. 2(a), the bar is fixed in a rigid frame. The bar is then subjected to a temperature load. It is heated uniformly from room temperature to a maximum temperature of 600 °C and then cooled back to room temperature (Fig. 2(b)).

Ignoring the creep and phase transformation strains, the total strain in the bar can be expressed as:

$$\boldsymbol{\varepsilon}^{total} = \boldsymbol{\varepsilon}^{elastic} + \boldsymbol{\varepsilon}^{plastic} + \boldsymbol{\varepsilon}^{thermal} \quad , \tag{1}$$

where $\boldsymbol{\varepsilon}^{elastic}$, $\boldsymbol{\varepsilon}^{plastic}$, and $\boldsymbol{\varepsilon}^{thermal}$ represent the elastic, plastic, and thermal strains, respectively. $\boldsymbol{\varepsilon}^{elastic}$ is determined from this relation, and then stresses can be computed using Hooke's law as follows:

$$\boldsymbol{\sigma} = \boldsymbol{D}\boldsymbol{\varepsilon}^{elastic}. \tag{2}$$

Fig. 2(c) shows a graph of the different strain measurements in the bar in the longitudinal direction while employing a temperature-independent material model. The thermal strain increases linearly with increasing temperature. As the bar was restrained in the longitudinal direction, the expanding material caused compressive strain in the bar. Initially, only compressive elastic strain appeared; however, as the material reached its elastic limit, compressive plastic yielding began. Both elastic and plastic strains continue to increase as the thermal strain increases. After the thermal strain starts to decrease, the elastic strain first shows a decreasing trend and then becomes tensile. During the decrease and reversal of the elastic strain, the plastic strain remains constant. With a further decrease in the thermal strain, the material reaches its elastic limit and starts yielding under tension. This yielding under tension causes a reduction in the magnitude of the plastic strain. As the bar is completely cooled, the thermal strain vanishes, and residual elastic and plastic strains develop in the material. This causes residual stresses in the material, even when the external excitation source is removed [25]. The residual elastic strain is tensile; hence, the residual stress is also tensile. Considering the force balance, the horizontal sides of the frame experience compressive stresses when the bar is cooled.

1.2. Formation mechanism of residual stresses

The analogy of a fixed bar can be used to explain the residual stresses in a layer-by-layer deposition manufacturing process [11,24]. Let us consider a simplified building process in which the material is deposited layer-by-layer on a substrate, as shown in Fig. 3. It was assumed that the existing part was at a uniform temperature, while the newly deposited layer was simultaneously heated. The higher temperature of the top layer caused the material to expand. However, this expansion is hindered by the lower layers, resulting in compressive stress in the top layer and tensile stress in the lower layers. During this expansion, the material in the top layer undergoes plastic yielding, as in the case of the bar (see Fig. 2). After the heat source is removed and the top layer is cooled, tensile stresses appear in the top layer, and compressive stresses in the lower layers. In Ref. [26], this mechanism is called the cooldown phase mechanism.

However, in reality, thermomechanical history is very complicated because new layers are not instantaneously heated. The heat source heats the feedstock material locally and the heated material tends to expand; however, this thermal expansion is confined by the surrounding material. This results in a compressive stress state and permanent plastic yielding in the heated zone (see Fig. 4). As the heat source moves away and this zone begins to cool, the material in this zone shrinks; however, this shrinkage is restrained by earlier plastic yielding [11]. This results in a residual tensile stress in this zone. These tensile stresses are balanced by the compressive zone, as shown in Fig. 4(b). These thermomechanical excitations cause the part to bend toward the heat source. This mechanism is referred to as the temperature gradient mechanism (TGM) in Ref. [11].

Because the heat source is constantly moving and the material undergoes heating–cooling cycles, the evolution of the stress–strain state is highly complex. Fig. 5 illustrates the stress–strain history induced at a material point (black dot) as the power source passes, as elaborated by Liang et al. [28]. It is assumed that the point is stress- and strain-free when the power source is placed on the position shown in configuration A. Owing to the temperature increase, the material expands and experiences compressive stresses because it is constrained by the surrounding material. This local expansion causes permanent deformation of the material. The maximum strain occurs when the power source is moved to the left, as shown in configuration B. As the power source moved further, the material point cooled and tensile stresses appeared. With further cooling and owing to the shrinkage of the surrounding material, the material point yields under tension. The tensile stresses reach the maximum point corresponding to configuration C.

1.3. Process dependencies

Several parameters and factors affect the generation and distribution of residual stress in AM-built parts. First, the component design and material selection have a significant impact on the residual stress and strain distributions [26]. The thermomechanical properties of the selected material (Young's modulus, yield strength, phase transformation temperature, thermal conductivity, coefficient of expansion, etc.) influence the temperature gradient and deformation of the part during the building process, which in turn affect the distribution of residual stress. Similarly, different regions of a part might experience different thermal gradients owing to, for example, different cross sections and/or the ability to conduct heat to the base plate, which again affects the distribution of residual stress.

In addition to the part design and material, the process parameters and scanning strategy used to build a part considerably affect the distribution of residual stress and distortion. By increasing the power level of the heat source, a higher relative density can be achieved in the built part [29]. Wang et al. [30] reported that the relative density of a bulk sample first increases and then decreases with increasing energy density. Furthermore, the yield and tensile strengths decrease with an increase

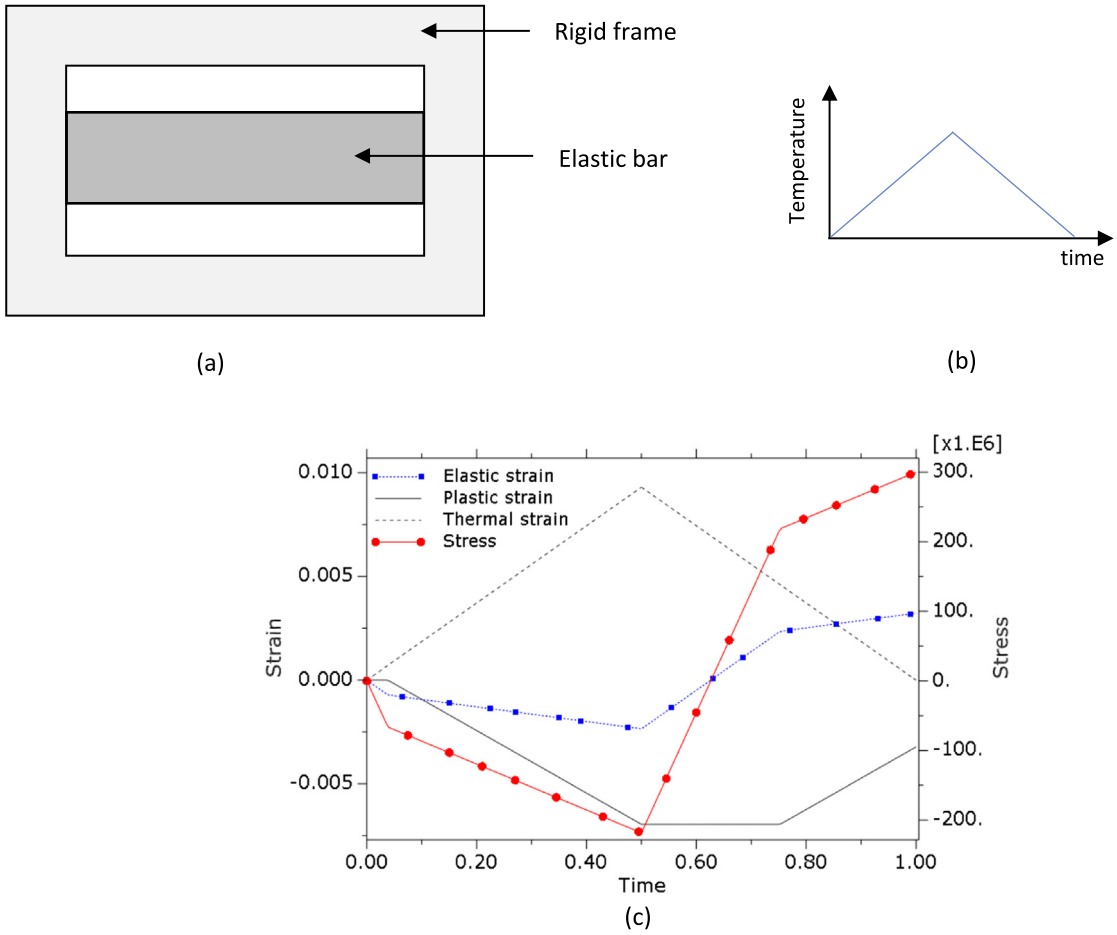

Fig. 2. (a) A bar fixed in a rigid frame to illustrate the origin of residual stresses; (b) Temperature load; (c) Evolution of different strain measures with time when the bar is subjected to the temperature load.

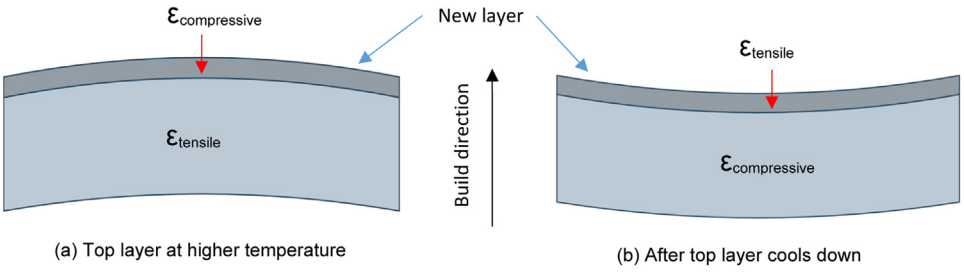

Fig. 3. Schematic of the origin of residual stress in the AM process according to Ref. [24].

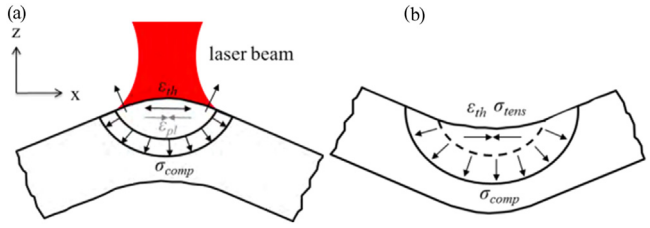

Fig. 4. Origin of residual stresses in AM structures: (a) Heating by power source; (b) After cooling [27].

in the power of the heat source [31,32]. Mukherjee et al. [33] reported that distortion increased almost linearly with power. This was attributed to the observation that a higher heat input results in a larger melt pool, which results in larger distortion during solidification. It has been shown that the higher the energy input, the larger the residual stress produced [34]. However, other studies have reported that the maximum residual stress decreases with an increase in the energy input [35].

Scanning speed is also an important process parameter that has a significant effect on residual stresses and distortion. A lower scanning speed increases the elongation to failure [32]. Mukherjee et al. [33] reported that distortion decreases with an increase in scanning speed. Shiomi et al. [36] found that the residual stress first decreases and then increases with increasing scan speed. Xiao et al. [37] inferred that, although the process parameters affect the residual stress, no clear conclusion can be drawn regarding the relationship between the process parameters and the induced residual stress. Furthermore, the complex relationship between the residual stress and process parameters is likely responsible for the conflicting results reported in the literature.

Various scanning strategies can be used to produce these components. Scanning strategy refers to a pattern in which a heat source moves over a substrate. The choice of the scanning strategy method has been found to have a significant impact on the residual stresses and distortion [38–41]. The scanning strategy affects the thermal history, which con-

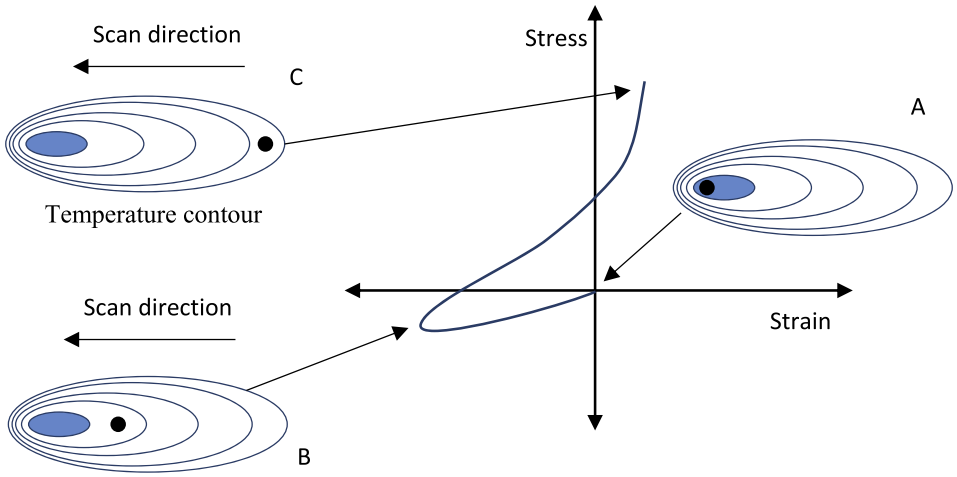

Fig. 5. Schematic illustration of residual stress generated at a point during power source scanning [28].

sequently affects the solidification pattern. Consequently, components with similar geometries fabricated using different scanning strategies can exhibit completely different physical properties.

The physical properties of a material depend on its microstructures. In metal alloys, the microstructure is characterized by the number of phases, their proportions, and distribution. Microstructure formation depends on the alloying elements, their concentrations, and the thermal history to which the material has been subjected. As the consolidated material in an additively manufactured part undergoes heating and cooling cycles, its microstructure undergoes several changes. The process parameters utilized to produce a component influence the thermal cycle experienced by the material and, consequently, control the microstructure. Diverse phases can be present in AM-fabricated structures because of their very high spatial and temporal temperature gradients. Hence, knowledge of the phase fractions is required for more accurate residual stress and strain predictions.

The residual stresses in a part built using an AM process can lead to part distortion, loss of geometric tolerance, and detrimental effects on fatigue performance [11,42]. Thus, residual pressures can affect not only the behavior but also the longevity of a component. Several post-build treatments are available to mitigate the residual stress, such as hot isostatic pressing [43,44]. However, these treatments increase production costs and, in some cases, are impractical because of the complex shapes and geometric precision required. The preferred approach to address this problem is to determine an optimal build plan that minimizes the residual stress formation and part distortion [45,46]. Understanding the relationship between the processing parameters and the properties of the final part is challenging because of the complex thermal phenomena that occur during the AM process. Experimental trial runs are a common practice for determining the optimal process parameters; however, they are time-consuming and expensive [1]. Numerical models have also been extensively used to shed light on how process parameters influence the AM process. Because the physics governing the AM process is considerably complex, it is impractical to capture all aspects of the process using one model. Therefore, modeling of AM-related phenomena was performed at different length scales. For example, such models can be used to model heat source and feedstock interaction, phase changes, melt pool size, and grain evolution [47].

Part-scale models are used to study the global behavior of the components. Such a model is used to predict the residual-stress development and deformation as a function of the process parameters. Modeling phenomena, such as grain structure formation, melt pool size, and microstructure evolution [46], are of little or no interest in modeling part-level behavior. In addition, considering the required computational resources, a single model that captures all aspects of the process is not feasible. Therefore, such phenomena are ignored in the part-scale model. However, to realistically predict the global behavior, a part-scale model should account for all phenomena involved in the AM process [46]. In general, reductions in part-level models are introduced for the time-efficient prediction of global behavior [8], for example, the laser-material interaction is ignored; instead, a heat source model is used to approximate the transient heat transfer mechanism at the molten pool. Some engineering judgments ignore phenomena with insignificant effects. The goal is to simulate the problem with minimum computational resources while retaining sufficient physical fidelity to ensure confidence in the analysis results.

Several researchers have developed numerical models based on the finite element (FE) method to predict the thermal and mechanical behaviors of built components [48]. Such models typically involve material-state transition, incremental addition of feedstock material, transient heat transfer, realistic material models, and heat source modeling. A thermomechanical model involving a moving heat source is considered a high-fidelity model.

Many deposited layers are typically represented by a single layer in an FE model to reduce the total number of degrees of freedom in a high-fidelity model. This is called “layer lumping” or “layer agglomeration” [49,50]. Adaptive remeshing techniques have also been used with high-fidelity models with the aim of achieving fewer DoFs while retaining accuracy. This technique alters the element size, such as to have a fine mesh in regions where the solution gradients are high and a coarser mesh in regions where the solution gradients are low [51]. Even after introducing these reductions and enhancements, high-fidelity models remain computationally expensive, hindering their large-scale adaptability. To further reduce the computational resources required to simulate part-scale behavior, radical assumptions are introduced to develop simpler models. In simplified models, a complete layer is typically subjected to a uniform load (e.g., strain, heat flux, or temperature field) instead of a moving heat source. Several simplified models have been developed to rapidly simulate part-scale behavior. These models yield quicker results at the cost of accuracy loss. Layer lumping was used in most studies involving simplified models [52,53]. By adopting simplified modes, the computational times are significantly reduced, which makes the AM process simulation of engineering components feasible.

Several studies have reviewed the residual stress measurement techniques, formation mechanisms, modeling approaches used for prediction, and process parameter dependencies. In 2014, King et al. [54] provided an overview of the modeling and simulation of the PBF process at the Lawrence Livermore National Laboratory. In 2016, Megahed et al. [46] surveyed the modeling approaches used for residual stress prediction. They discussed the models required to encompass a range of AM processes with different lengths and timescales. In another study published in 2016, Markl and Körner [55] reviewed numerical modeling

approaches on multiple length scales and timescales to describe different aspects of PBF processes. In 2017, Meier et al. [56] reviewed modeling and numerical solution procedures for PBF processes. They also reviewed experimental studies that are important for understanding thermophysical mechanisms. Bartlett and Li [24] in 2018 reviewed the literature and described the background mechanics for residual stress development along with the methods of measurement. They also reviewed the modeling techniques and in-process experimental measurements. In 2018, Luo and Zhao [57] summarized FE models used in the simulation of the PBF process. They also discussed the simulation techniques used to reduce the computational costs. Bertini et al. [58] in 2019 reviewed numerical models aimed at predicting the residual stress–strain fields. Debroy et al. [59] in 2018 comprehensively reviewed the AM of metallic components and discussed the origin of residual stress. They also summarized the thermal and structural analyses reported in the literature. Recently, Wei et al. [60] provided an excellent review of the mechanistic models used to model various AM phenomena. The solidification, residual stresses, distortion, formation of defects, and evolution of microstructures and properties were critically reviewed. Bayat et al. [61] presented a review of numerical simulations for AM with a focus on mesoscale models. The study also discusses different classes of computational fluid dynamics (CFD) models for investigating melt pools. However, they do not describe any model in detail. Chen et al. [26] reviewed residual stress in AM with a focus on the formation mechanism, process parameter dependencies, prediction, and control methods. Xie et al. [62] wrote a review paper detailing the evolution of distortion and residual stresses for various AM processes. They also described the factors influencing residual stress. Qin et al. [63] reviewed the formation mechanism of geometrical defects, including the distortion and delamination of parts manufactured using the DED process. They also discussed product design adjustments to compensate for material shrinkage and distortion.

The aforementioned reviews have either become outdated or do not focus entirely on the modeling of residual stresses. In this paper, a review of the latest papers published on modeling approaches used for the simulation of residual stress and deformation during the AM build process is presented. Both high-fidelity and simplified models described in the literature were reviewed. The remainder of this paper is divided into seven sections. In the second section, the major elements of the high-fidelity model are described. In the third section, the two popular simplified models are described in detail. The fourth section discusses data-driven approaches to residual stress and distortion in AM. In the fifth section, measurement techniques used to validate numerical approaches are presented. The sixth section, titled miscellaneous, covers topics that did not fit into the previous sections. Finally, concluding remarks are presented.

2. High-fidelity Models

High-fidelity models involve a moving heat source, and the incremental addition of a material as a part is performed pass-by-pass and layer-by-layer. The major aspects of a high-fidelity model are the heat source model, material deposition techniques, layer lumping, thermal stress analysis, adaptive meshing techniques, powder-to-solid transition, solid-state phase transformation, material models, and scanning strategy.

2.1. Heat source model

All AM processes involve a heat source that melts the feedstock material locally. Melting of the feedstock material occurs on the front side of the melt pool, whereas solidification occurs on the back side of the pool, creating a fusion zone (FZ). The nonmelted area of the adjacent material that has undergone changes in material properties caused by exposure to high temperatures is called the heat-affected zone (HAZ). High temperatures can cause solid-state transformations in the HAZ.

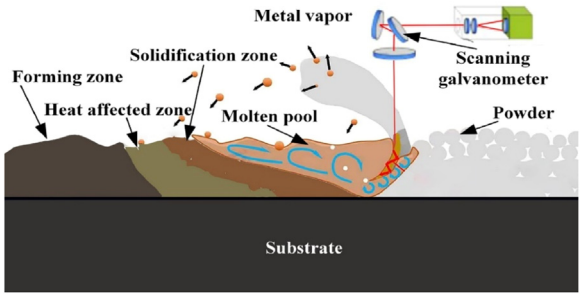

Fig. 6. Schematic illustration of the melt-pool formed during the PBF process [65].

Molten metal convection and solidification render melt-pool physics a cumbersome task to model. A schematic illustration of the melt pool formed during PBF is shown in Fig. 6. In a part-level thermomechanical model, such complex phenomena are not directly simulated; instead, a heat flux distribution is specified to approximate the power source and feedstock interactions [59]. Various heat source models that specify different heat flux distributions have been reported in the literature. A heat source model specifies how much of the heat source power is used to heat the feedstock material and how this heat is distributed [64]. Issues such as the interactions between the melt pool and heat source spot, varying radiation properties of the build surface, and penetration depth of the heat source into the build are some of the physical phenomena that a heat source model can be used to estimate in a part-scale model using empirical data [64].

Heat source models for AM are often derived from welding literature. They are categorized into point, line, surface, and volumetric heat sources. Both surface and volumetric heat source models have been widely used for modeling of the AM processes. Surface heat source models assume that heat is distributed along the deposition surface with no heat penetration beneath the surface and ignore the digging action of the heat source that transports the heat well below the surface [66]. Volumetric heat source models consider the heat penetration beneath the surface of the material. The following is a brief description of the heat source models found in the AM literature. A detailed discussion of the heat source models is provided in Refs. [64,67,68]. Some of the most popular heat source models are as follows.

Gaussian surface flux model

One of the earliest models for heat distribution in welding problems assumed a uniform power density distribution. This model does not provide satisfactory results from either physical or numerical perspectives. Physically, the results do not relate well to the observed phenomena, and numerically, this assumption requires a fine mesh density to consider the power density step at the boundary [66]. To address these issues, a Gaussian distribution of heat flux [66] over the surface was assumed, as shown in Fig. 7.

A Gaussian heat distribution can be expressed as:

$$q(r) = q_{\max} \exp\left(-kr^2\right), \tag{3}$$

where $q_{\max}$ is the maximum heat flux, k is the concentration factor, and r is the radial distance from the center of the heat source. By assuming that 95% of the thermal heat is absorbed within the radius of the heat source spot, heat flux can be written as:

$$q(r) = \frac{3Q}{\pi r_s^2} \exp\left(-\frac{3r^2}{r_s^2}\right),$$

where Q is the effective power of the heat source and r_s is the maximum radius of the heat source spot. In a coordinate system that moves with the heat source, the above equation can be expressed as:

$$q(x,\xi) = \frac{3Q}{\pi r_s^2} \exp\left(-\frac{3x^2}{r_s^2} - \frac{3\xi^2}{r_s^2}\right).$$

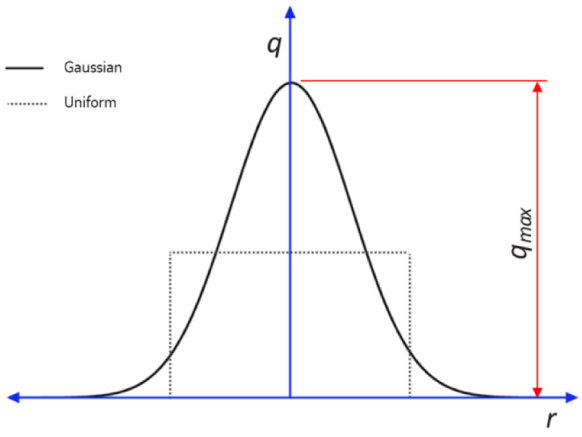

Fig. 7. Distribution of a Gaussian heat source.

In this model, the heat intensity at the edges of the heat source spot is considerably less than the maximum heat intensity, which is preferable numerically, as with the constant power density, an FE model requires an excessively finer mesh to consider the thermal impulse at the edge of the spot [64]. When the penetration depth of the heat flux is small, the Gaussian surface flux model yields acceptable results. Because a laser heat source cannot penetrate a material deeply [57], it has been modeled as a surface flux in several works [10,69]. An electron beam can penetrate a material considerably deeper than a laser beam; therefore, surface heat sources are not considered suitable [57].

Hemispherical power density model

For high-power heat sources, the digging action becomes significant and a volumetric model is necessary. The hemispherical Gaussian distribution of heat density is an extension of the Gaussian surface flux model, which considers heat penetration beneath the surface. The heat distribution for the hemispherical Gaussian model can be expressed as:

$$q(x,y,\xi)=\frac{6\sqrt{3}Q}{\pi\sqrt{\pi}r_s^3}\exp\left(-\frac{3x^2}{r_s^2}-\frac{3y^2}{r_s^2}-\frac{3\xi^2}{r_s^2}\right).$$

Ellipsoidal power density model

The melt pool around several heat sources is far from spherical in shape. Therefore, an ellipsoidal power density model was proposed [66], which presents a more generalized formulation. It assumes a Gaussian distribution on an ellipsoid. The heat distribution for the ellipsoidal power density model can be expressed as:

$$q(x,y,\xi)=\frac{6\sqrt{3}Q}{\pi\sqrt{\pi}abc}\exp\left(-\frac{3x^2}{a^2}-\frac{3y^2}{b^2}-\frac{3\xi^2}{c^2}\right),$$

where a, b, and c represent the lengths of the semiaxes. Generally, a is taken as the half-width of the deposition, and b is the melt pool depth [70].

Double ellipsoidal model

This model is based on the work of Goldak et al. [66]. In this model, the power density of the region in front of the heat source center and behind the heat source center is defined separately, which allows the modeling of asymmetries in the heat distribution over the melt pool. Two different ellipsoidal sources are combined, providing considerable flexibility in specifying the power density distribution. The front half is the quadrant of one ellipsoid, and the rear half is the quadrant of another ellipsoid. This model enables the consideration of different temperature gradients at the front and trailing sides of an experimentally observed heat source. The heat density distributions for the front and rear quadrants are expressed as follows:

$$q(x,y,\xi)=\frac{6\sqrt{3}f_fQ}{\pi\sqrt{\pi}abc_f}\exp\left(-\frac{3x^2}{a^2}-\frac{3y^2}{b^2}-\frac{3\xi^2}{c_f^2}\right),$$

$$q(x,y,\xi)=\frac{6\sqrt{3}f_rQ}{\pi\sqrt{\pi}abc_r}\exp\left(-\frac{3x^2}{a^2}-\frac{3y^2}{b^2}-\frac{3\xi^2}{c_r^2}\right),$$

where c_f and c_r represent the lengths of the semi-axes of the front and rear ellipsoids, respectively. Q is the effective power of the heat source and r_s is the maximum radius of the heat source spot. f_f and f_r represent the fractions of heat deposited in the front and rear quadrants, respectively, where $f_f+f_r=2$.

Physically, c_f and c_r represent the radial dimensions of the molten zone at the front and rear of the heat source [66]. If the size of the molten zone is known from the experiment, this information can be used to determine the lengths of the semi-axes. In the absence of experimental data, c_f is assumed to be equal to a and c_r to $2a$ in the first approximation [66].

Conical heat source model

The conical heat source model is a volumetric model that has been used in welding simulations [71–73]. The heat deposition area is maximized at the top and decreases with increasing depth. In other words, as the depth increases, the diameter of the heat-density distribution region decreases linearly. However, the heat density along the central axis remains constant. In any plane perpendicular to the z axis, the heat density is given by a Gaussian distribution. The power density distribution for the conical power density model can be expressed as:

$$q(r,z)=q_{\max}\exp\left(-\frac{3r^2}{r_0^2}\right),$$

where $q_{\max}$ is the maximum heat flux, r_0 is the distribution parameter, and r is the radial distance of any point from the center of the heat source.

Line heat input model

This model was developed for powder-bed AM by Irwin and Michaleris [70]. To simulate the movement of a heat source accurately, the time increments must be sufficiently small such that the source moves a distance smaller than its radius during each increment [74]. Consequently, very small time steps are required to accurately model the motion of the heat source when the source radius is small. This requires significant computational resources to model PBF systems. Aliasing may occur if the time increments are large. The line heat input model addresses this problem by averaging the heat sources along the path. The averaged heat input over the period of a time step Δt can be expressed as [69]:

$$\bar{q}(x,\xi,t)=\frac{1}{\Delta t}\int_{t_0}^{t_0+\Delta t}q(x,\xi)\mathrm{d}t.$$

The scan path is broken into several small linear segments, each of which is simulated in one-time increments. This results in considerably shorter computation times. However, the lengths of these linear segments cannot be large; otherwise, a significant amount of error will be introduced. To overcome this issue, a hybrid approach was proposed in Ref. [69] in which a moving Gaussian surface heat source was applied along with a line heat input for each scan track. It was demonstrated that the hybrid approach could be adapted to significantly reduce the simulation time without sacrificing excessive accuracy.

In general, three methods can be employed for estimating the parameters in a heat source model [75]:

① Temperature can be measured using thermocouples at selected points. Subsequently, an FE analysis was performed alliteratively to fit the parameters such that the predicted temperatures matched the measurements at specific points.

②The residual stress or strain can be measured using any measurement technique (e.g., hole drilling, neutron diffraction, or X-ray diffraction). Subsequently, FE analysis was performed iteratively to fit the parameters such that the predicted residual stresses matched the measured stress or strain data.

③Macrographs of cross-sections of deposition can be prepared. The parameters are then simulated iteratively such that the geometric appearance of the fusion zone, molten pool, and heat-affected zone (HAZ) match the dimensions in the macrograph [76].

Owing to the complexity of the AM process, determining whether a heat source model functions well within a high-fidelity model can be challenging. The high-fidelity model involves several experimentally established assumptions and empirical constants. In the presence of several factors, it is challenging to determine the validity of a heat source model. Therefore, a heat source model must be validated separately before being incorporated into a high-fidelity model [64].

Heat source modeling for PBF

Different heat-source models have been used to model the PBF process. A laser beam can only penetrate a solid material up to several micrometers; therefore, it has been modeled in several studies as a surface heat source to speed up the analysis [77]. However, volumetric heat sources are preferred for accurate analysis [78]. The electron beam has a considerably higher energy density, which results in a much deeper penetration of the solid material [79]. Therefore, an electron beam is typically modeled using a volumetric heat source [77]. Tran and Lo [80] performed heat transfer simulations using a novel volumetric heat source based on a Gaussian distribution to estimate the size of the melt pool cross-section during the laser PBF process. They reported that the predicted peak temperature in the melt pool approximated the measured value. Furthermore, good agreement was observed between the computed melt-pool dimensions and measurements. Foroozmehr et al. [81] used a volumetric heat source model with a uniform distribution to predict the melt pool size. Experiments were conducted to calibrate the effective optical penetration depth of the laser beam into the powder bed. The predicted melt-pool depths were validated using the experimental results. Zhang et al. [73] developed a finite element model for the laser PBF process to predict the melt pool dimensions. Eight different heat source models published in the literature were tested for the numerical modeling. All the heat source models led to over 40% shallower melt pools compared to the experiments. To improve the simulation results, a new model with varied anisotropically enhanced thermal conductivities and absorptivities was proposed. The average errors in melt pool width and depth reduced by 2.9% and 7.3%, respectively. Galati et al. [82] developed a thermal numerical model for an electron-beam PBF process. They ignored the penetration depth of the electron beam and approximated the heat flux as a uniform circular distribution at the top surface. Zäh and Lutzman [79] used a Gaussian volumetric distribution to model a heat source and simulate an electron-beam PBF process. The model was validated by comparing the predicted temperature with the temperature measured using a thermocouple. Yue et al. [83] developed a thermomechanical model to simulate the molten pool evolution and residual stress distribution in the electron-beam PBF process. The Goldak volumetric distribution was used to model the heat source.

Heat source modeling for DED

Similar to the PBF process, various heat source models have been used to model the DED process. The simplest model specifies that the temperature of the newly deposited material should be equal to the melting temperature instead of employing heat flux [84,85]. This is based on the assumption that the material reaches its melting temperature upon reaching the surface of the part. In other studies [86,87], a surface heat flux was adopted to model the heat source. However, volumetric heat source models are considered to be the most accurate. Yang et al. [88] developed a FE model to investigate the thermomechanical behavior of a part built using the LENS-directed energy deposition process. An ellipsoidal volumetric heat-flux model was used. The model was validated by comparing the simulated distortion of the substrate with experimental measurements. Ding et al. [89] modeled the heat source as a well-distributed volumetric heat input for a part built using a wire arc AM process. The model was insensitive to the mesh, which significantly reduced the computational time. The computed temperature history and distribution were validated by comparison with the measurements from thermocouples and a thermal imaging camera. Giarollo et al. [90] proposed a double bi-ellipsoid heat source model for the wire-arch AM process and compared the numerical results with those of the Goldak double-ellipsoid model. They concluded that the double bi-ellipsoid model describes the observed geometry in macrographs more accurately than the Goldak double-ellipsoid model.

2.2. Material deposition modeling

In the metal manufacturing process, parts are produced pass-by-pass and layer-by-layer. Incremental addition of the material is the most challenging aspect in the numerical modeling of residual stresses and distortion and requires special techniques in numerical analysis. The available techniques mainly depend on the type of AM process being modeled. During the PBF process, a layer of powder is spread over the build area, and an energy source scans specific areas according to the CAD geometry. Thus, a layer could consist of both powder and solidified material. The presence of a preplaced powder layer on the powder bed requires special treatment because the solidified material and powder particles have different thermal and mechanical properties. During the DED process, an energy source fuses the material as it is being deposited; therefore, the computational domain includes only the deposited material and no powder [91].

FE analysis can be performed in either an Eulerian or a Lagrangian framework. In a traditional Lagrangian analysis, the nodes are fixed within the material, and the elements deform as the material deforms. Lagrangian elements are always 100% full of a single material, so the material boundary coincides with the element boundary. In contrast, in Eulerian analysis, nodes are fixed in space, and material flows through elements that do not deform. Eulerian elements may not always be 100% full of materials. The Eulerian formulation trades accuracy for robustness. Finite element discretization based on the Lagrangian framework is commonly used for metal AM processes [92]. Ding et al. implemented a Eulerian framework to simulate the AM process. It required fewer computational resources than the Lagrangian formulation but was limited to simpler geometries. In the following sections, all the discussions are related to the Lagrangian framework.

Powders are the most commonly used feedstock materials in AM. The powder material consists of a multitude of particles of different sizes and porosity. Modeling a large number of particles requires enormous computational resources [55]. For part-scale models, a common approach to reduce computational effort is to approximate the powder as a continuum with homogenized properties. In such models, the powder is represented as a reduced-density, low-strength solid [93]. Previous studies have shown that in thermal calculations, the metal powder can be considered as a continuum with sufficient accuracy [79,94].

Material deposition modeling requires special methods for handling elements as new materials are added to the built domain. The techniques for the PBF and DED processes are quite different because of the fundamental differences in material deposition. The techniques used to model the DED process are also described.

The techniques used to model material deposition in DED processes can be divided into three categories: (a) quiet element methods, (b) inactive element methods, and (c) hybrid activation method [59,95]. This is schematically illustrated in Fig. 8.

In the quiet element method, the final discretized geometry of the desired part is already present in the model prior to the simulation of the building process. As the material is deposited, real material prop-

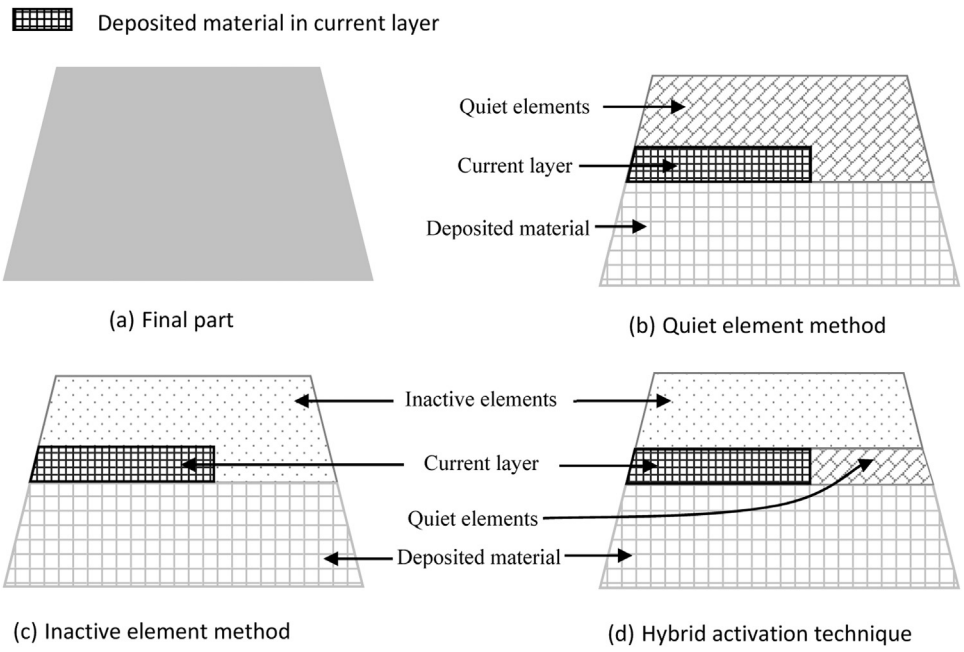

Fig. 8. Material deposition modeling techniques for the DED process.

erties are assigned to the elements representing the deposited material, whereas the material properties of the non-deposited elements are scaled down such that they have no or an insignificant effect on the analysis results. Hence, these nondeposited elements are called quiet elements. As the heat source passes over other elements, these elements are assigned real material properties. This method does not require the redefinition of a computational domain during the solution procedure.

In the inactive element method, only the elements representing the deposited material are present in the model. As the heat source moves and the material is deposited, new elements representing the deposited material are added. In other words, elements for the material yet to be deposited are not included in the solution domain at the beginning and are gradually born into the solution domain. This method is known as the "B-element birth method" [46,59]. This method makes the greatest physical sense.

The major advantage of using the quiet element method is that because the number of elements is constant, the number of equations does not change, and solver initialization during the simulation process is not required [95,96]. Furthermore, this method can be easily implemented using commercial finite element software. However, there are several quiet elements at the beginning of the deposition process that require solving a large number of equations even though only a small amount of material has been deposited. In other words, the DoF of the problem remains constant because the DoF associated with the quiet elements is always present in the system of equations. Furthermore, owing to the scaling down of material properties, the stiffness matrix can become ill-conditioned and convergence problems may occur [95]. However, if the material properties are not sufficiently scaled down, thermal energy enters the quiet elements, producing erroneous results [95].

The major advantage of using the inactive element method is that it does not require scaling factors to exclude elements from the analysis. Furthermore, the stiffness matrix was considerably smaller because only the elements representing the deposited material were considered. The stiffness matrix is also well defined because no scaling factor is used. However, this method requires the domain to be redefined during the solution procedure, and the elements must be renumbered, which increases the computational cost. This method is difficult to implement in commercial finite element solvers [95,96].

A hybrid activation method was proposed to exploit the strengths of both material deposition modeling methods [95]. In this method, the part is divided into layers. The current layer, which is built using a heat source, is modeled using the quiet-element method. This implies that the nondeposited material in the current layer is represented by quiet elements. As the heat source scans over the current layer, additional elements representing the newly deposited material are assigned to the real material properties. The nondeposited layers above the current layer are modeled using the inactive element method. Therefore, the elements in these nondeposited layers are not present in the model. After completing the scan of the current layer, the next layer is added to the model, and the elements are renumbered according to the inactive element method. By combining both the activation methods, an efficient and cost-effective solution can be achieved.

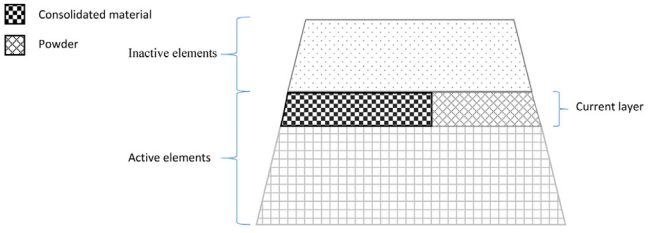

Fig. 9. Material deposition modeling technique for the PBF process.

The PBF process involves spreading the powder material over the previous layers. This can be modeled using the inactive element method [50], where a new layer of powder is represented by activating a complete layer of elements. These elements are initially assigned to the properties of the powdered material. As the heat source moves over the layer, the elements are heated above the liquidus temperature and assigned the material properties of the liquid material. Ultimately, these elements are assigned bulk material properties when their temperatures are below the solidus temperature. A schematic of this method is shown in Fig. 9. Notably, the material is represented as either a powder or consolidated state (solid and liquid materials together). After the laser scans the complete layer, a new layer of elements is activated. This process continues until a complete part is constructed [69].

2.3. Layer lumping

A high-fidelity model requires significant computational resources to predict the residual stress and strain. To minimize the total DoFs, several physical layers are represented by a single layer in the FE model.

In other words, several physical layers are lumped into a single computational layer. This enables the use of a relatively coarse FE mesh. Five different aspects/parameters must be considered when considering a layer lumping strategy for a problem [50]: (1) lumping ratio, (2) heat source size, (3) heat source power, (4) scan speed, and (5) inter-layer dwell.

The first consideration when implementing layer lumping is the lumping ratio, that is, the number of physical layers represented by a single numerical layer. A higher lumping ratio results in a more time-efficient analysis; however, the accuracy can suffer. A lumping ratio of 10 was used in Ref. [97] to obtain accurate results. A lumping ratio of 16.7 was used in Ref. [50], and good agreement was observed between the measured and simulated strains.

The second aspect to be considered is the size of the heat source. Ideally, it is scaled up by the lumping ratio such that it heats the entire agglomerated layer. This scale-up is called heat source agglomeration. Hodge et al. [49] implemented a model for predicting the residual stresses and distortions in several parts built using selective laser melting. An agglomerated laser heat source was used to scan each computational layer. Comparisons with the experimental results were generally encouraging. Ganeriwala et al. [50] used layer and heat source agglomeration to simulate the residual strains in a PBF-built part. Four parts with the same geometry were constructed using different scanning strategies. By comparing the predicted results with the X-ray diffraction measurements, it was concluded that the agglomeration techniques were unable to fully capture the scan strategy effects. It was also noted in Ref. [97] that the heat source model is not as important as the total magnitude of the heat flux [97]. In another study, Ganeriwala et al. [98] used layer and heat source agglomeration to simulate the residual strains in a PBF-built part at varying levels of layer height and mesh refinement. They reported a negligible decrease in accuracy for coarser meshes and concluded that more refined meshes alone are not sufficient for accurate predictions; however, material models representing the true behavior of the material are also required.

The third issue to be addressed is the correct power of the heat source. An obvious choice is to increase the power, such that the total energy input into the domain is conserved according to the number of physical layers represented by the numerical layer. However, this leads to the overheating of the domain [50]. This is because, in the actual process, heat is applied to a very small volume with continuous conduction to neighboring areas, and the material has time to cool down during inter-layer dwell. To address the overheating problem, tuning of the heat source power is required to make the maximum temperature realistic. In other studies [49,98,99], the power was increased heuristically to ensure complete melting of the agglomerated layers.

The fourth aspect that needs to be addressed is scan speed. In several works [50,98,99], the scan speed was specified to be equal to the physical process value. By maintaining a scan speed equal to the process speed, we attempted to conserve the characteristic heating time of an individual point [50].

The fifth aspect to consider is the total inter-layer time. In Refs. [50,99], the inter-layer time was scaled from the physical process value by the lumping ratio such that the total part building time was kept constant.

2.4. Thermal-stress analysis

The stress/deformation field in an additively manufactured structure depends on its temperature history. Ideally, such an analysis should be performed using fully coupled thermal stress analysis. A fully coupled analysis simultaneously solves the heat conduction and stress equilibrium equations. However, coupled analyses are computationally expensive. For problems in which the temperature field is almost independent of the deformation response, that is where the effect of mechanical deformation on the temperature field is negligible, a sequentially coupled approach can be used instead of a fully coupled approach. Sequential coupled analysis is typically more cost effective. However, the results may not be as accurate as those obtained using a fully coupled approach depending on the degree of coupling between the mechanical and temperature fields. A sequentially coupled analysis was performed by first conducting heat transfer analysis and determining the transient temperature field. In the second step, stress analysis was performed, and the temperature field as a function of time from the heat transfer analysis was imported as the thermal load. Therefore, the interactions between the temperature and deformation fields were not considered in the sequentially coupled analysis.

Sequentially coupled analysis

Sequentially coupled analyses have been used in several studies to simulate the PBF processes. Yang et al. [97] adopted a sequentially coupled thermomechanical approach to simulate residual strains in a laser PBF-fabricated part. A DELMIA powder bed fabrication application was used to generate the slicing and laser trajectories of the built part for analysis, according to the actual scanning strategy. A good correlation was observed between the predicted strain field and X-ray diffraction measurements of the built part. Similarly, to simulate residual stress and distortion in a laser PBF-fabricated part, Williams et al. [100] used a sequentially coupled thermomechanical approach. They applied a uniform temperature field instead of a heat flux as a load to a fraction of the layer to perform thermal analysis. The predicted distortion of the bridge shaped part was within 5% of the experimental measurements. Hussein et al. [10] used a sequentially coupled thermomechanical approach to study the temperature distribution, thermal stresses, and melt-pool dimensions in a single layer built on a powder bed. Laser energy density was applied as a volumetric Gaussian heat source. The simulation results revealed the magnitudes of the temperature and stress at different locations in the layer. Cheng et al. [101] used a sequentially coupled thermomechanical model to evaluate the effects of different scanning strategies on the temperature, stress, and deformation of the laser-PBF process. The model incorporated a volumetric Gaussian heat source and simulated the stress and deformation of the multilayer deposition.

Sequential coupling analysis has been used in several studies to simulate the DED process. Denlinger and Michaleris [102] used a sequentially coupled thermomechanical approach to study the influence of inter layer dwell time on the distortion of a DED-built part. Single-wall structures were fabricated on a substrate of a similar material using a laser DED process. The laser heat source was modeled using the Goldak double ellipsoid model. The in situ temperature, in situ distortion, and post-process residual stress predictions were compared with experimental measurements. Yang et al. [88] adopted a sequentially coupled approach to predict the thermomechanical behavior of a part built using laser DED. Five layers of rectangular contours of Ti-6Al-4V were deposited on a substrate of the same material. The substrate was clamped at one end using an aluminum fixture fixed to the table. An ellipsoidal heat-source model was employed for the numerical study. The thermal analysis was validated by comparing the temperature history at fixed points with the temperature measured using thermocouples. The mechanical simulation was validated by comparing the distortion magnitude of the substrate with experimental observations. Yan et al. [103] investigated the residual stress and warping of a stiffened panel produced by electron-beam freeform fabrication (wire DED process). The panel was analyzed using a sequentially coupled thermomechanical approach. The elements in the layer were sequentially activated according to the scanning path. Instead of specifying a heat source model, body heat flux was applied to each newly activated element. In each thermal analysis step, only one element was activated and body heat flux was applied. The predicted distortion agreed reasonably well with the experimental results.

Fully coupled analysis

Fully coupled analyses have been used by only a few researchers in AM process simulations. Strantza et al. [99] simulated the PBF build-

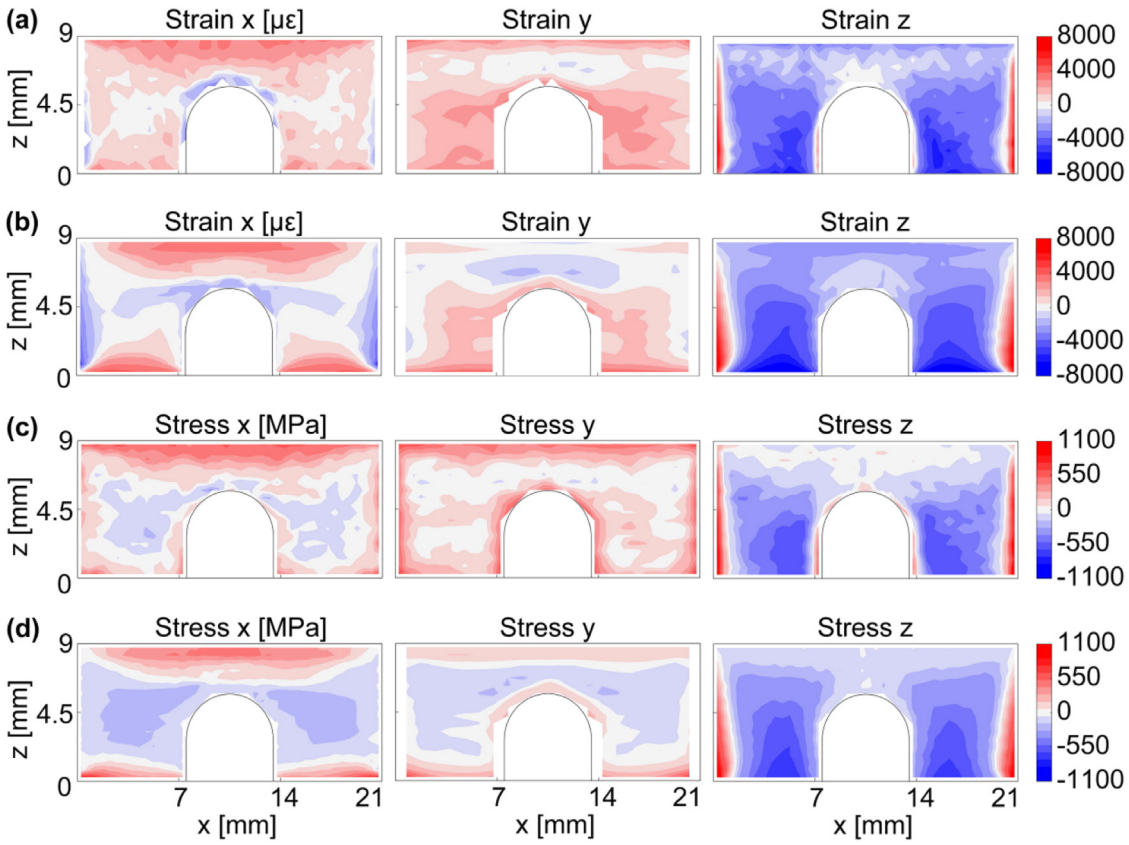

Fig. 10. Contour plots of the middle cross-section of a bridge-shaped specimen for the *x, y*, and *z* components: (a) Measured residual strain; (b) Simulated residual strain; (c) Measured residual stress; (d) Simulated residual stress [99].

ing process of a bridge-shaped component by adopting a layer and heat source agglomeration in a fully coupled model. They compared their predictions with X-ray diffraction measurements and found a good correlation between them. Fig. 10 compares the contour plots of the residual strain and stress obtained from the simulations and measurements. Ganeriwala et al. [50] implemented a fully coupled thermomechanical model to predict the residual stress during laser PBF. Good qualitative agreement was observed between the predicted strain field and synchrotron X-ray diffraction measurements of the built part. Riedlbauer et al. [104] developed a thermomechanical model to simulate the melting process. They focused on the performance considerations of the two solution approaches for thermomechanically coupled problems. A straight scanning path was simulated and the performances of the two algorithms were compared.

For AM process simulations, sequentially coupled analysis has been used in most studies because it provides a cost-effective solution, despite some loss of accuracy [105].

2.5. Adaptive meshing technique

Part-scale FE models are powerful tools for accurately predicting the residual-stress distribution in parts built using additive-manufacturing processes. A highly concentrated heat source requires the mesh to be refined to capture the high temperature gradient at the location of the heat source spot. As the heat source scans each layer pass-by-pass, the built part is discretized with a fine element density to capture high gradients. Conventionally, a part is discretized before the analysis and remains unchanged throughout the analysis. For large parts with fine element density, the degrees of freedom increase substantially, which makes FE analysis prohibitively expensive.

Adaptive remeshing techniques have been used to build FE models with a low DoF and sufficient accuracy. The objective of this technique is to obtain a fine mesh in a region where the thermal and stress gradients are high and a coarser mesh in a region where the gradients are low [51]. In other words, the mesh refinement is determined based on variations across domains [106]. Because the gradients are smaller for the layers away from the layer being built, these regions can have coarser mesh sizes. Thus, models with large spatial dimensions with respect to the size of the heat source can be analyzed accurately without considerably increasing the total number of DoFs. Different strategies are available for adaptive remeshing and have been implemented by researchers in the AM process. One approach involves merging the elements in the lower layers of a part while maintaining a higher density of elements in the top layers [92]. As more layers were added to the top of the built part, the mesh in the lower layers progressively coarsened. This results in a substantial increase in computational efficiency.

Patil et al. [106] presented a dynamic adaptive mesh refinement (AMR) and de-refinement method for time-dependent dynamic problems in which the mesh is dynamically adapted to new boundary conditions, evolving constitutive laws, or geometries. They applied this method to a metal laser-sintering process. This shows significant potential for efficient and high-resolution simulations. Gouge et al. [107] used H–Octree adaptivity, which combines eight adjacent elements into a single larger element. Their algorithm allowed adaptivity only between layers and not within a single layer. The number of fine top layers was used to determine how far away from the current layer the mesh was coarsened. Remeshing occurred after the addition of a new layer of elements. Ganeriwala et al. [98] used a mesh refinement scheme based on error estimators to simulate a single-track deposition. Refinement occurred for the elements closest to the moving laser beam. After the laser passed

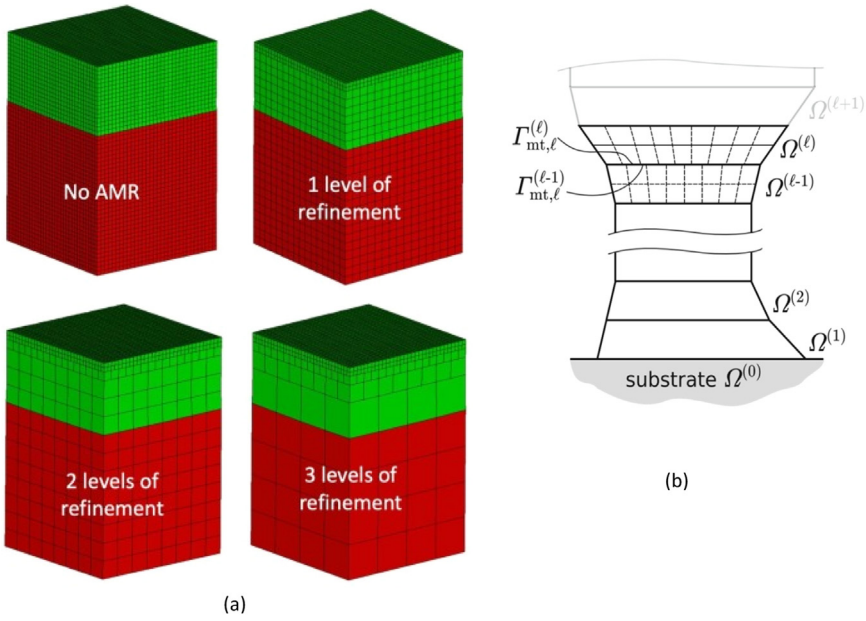

Fig. 11. (a) Demonstration of adaptive mesh refinement using a 1 mm × 1 mm cross-sectional domain, fully refined mesh (top left), mesh with 1 (top right), 2 (bottom left), and 3 (bottom right) levels of de-refinements, red elements represent the substrate, where green elements represent initially powdered material [98]; (b) Multilayer mesh tying concept [108].

away and the elements were cooled to room temperature, they were de-refined. They also used a layer-wise technique for part-scale models to increase the efficiency of the refining/de-refining processes. Elements in the current layer were not refined/de-refined as a function of the laser position, as it would add the expense of remeshing every time step or every few time steps, as opposed to once per layer. The de-refinement was based on the distance from the top surface of the part. Refinement and/or de-refinement occurred immediately after the deposition of a new layer. Fig. 11(a) shows the remeshing of a domain using this algorithm. Initially, the domain comprised a fully refined mesh with 16 powder layers (green). Only two layers were set to remain at the most refined level after de-refinement. After the three levels of de-refinement, the total DoFs decreased considerably. Proell et al. [108] proposed a dual-mortar mesh tying scheme to simplify the mesh generation. This scheme was used in a thermomechanically coupled FE model to simulate residual stress in a PBF-built part. This allows for nonconforming meshes between subsequent layers, as shown in Fig. 11(b). Traditional mesh-generation schemes require matching meshes between layers, which can result in distorted elements or large differences in nearby element sizes. The dual-mortar mesh tying scheme allowed for undistorted and almost equally sized elements, resulting in a reduced DoF. Another advantage of the dual mortar mesh tying scheme is the optimal convergence rate in the L^2-norm, which is generally not certain by other methods, such as collocation-type and mesh-tying methods [108,109].

2.6. Powder-to-solid transition

As the heat source scans the feedstock material, it undergoes a solid–liquid–solid transition. Therefore, special techniques are required to model this transition. Metal powders are the most common feedstock used in metal AM, so the discussion in this section is confined to them.

Feedstock materials can exist in three states: powder, liquid, or solid. A one-way change occurs during consolidation from powder to liquid, but the transition is bidirectional between the solid and liquid phases. This is schematically shown in Fig. 12.

Latent heat, that is, the energy absorbed or released during a change of state, is an important consideration in numerical modeling. In pure materials, this change occurs at a fixed melting temperature, that is, it is an isothermal state change. For alloys, the change in state typically occurs over a narrow temperature interval between the solidus temperature, T_s, and the liquidus temperatures, T_l [110]. This interval is referred to as the "mushy zone." Fig. 13(a) shows a typical temperature-enthalpy relationship for a nonisothermal phase change. Several methods are available to model the latent heat effects, such as the apparent heat capacity, effective capacity, and enthalpy methods.

Apparent heat capacity method

In this method, the latent heat is accounted for by increasing the heat capacity of the material in the state transition temperature range, that is, between the solidus and liquidus temperatures [111]. Fig. 13(b) schematically illustrates the apparent heat capacity calculation. The apparent heat capacity can be expressed as:

$$C_{app} = \begin{cases} C_s & T < T_{s,} \\ C_{in} & T_s < T < T_l, \\ C_l & T > T_l, \end{cases} \tag{4}$$

where C_s is the heat capacity of the solid state and C_l is the heat capacity of the liquid state. C_{in} epresents the artificially increased heat capacity of the material to account for the latent heat in the mushy zone, and is given by Eq. (5).

$$C_{in} = \frac{\left\{ \int_{T_s}^{T_l} C(T)\mathrm{d}T + H_f \right\}}{(T_l - T_s)}, \tag{5}$$

where H_f is the latent heat of the material.

A drawback of this method is that if, for example, for a melting case, the temperature of a point rises from below the solidus temperature to above the liquidus temperature in one time increment, latent heat is not accounted for in the control volume [111]. Therefore, small time increments are used to ensure that the temperature change does not exceed this interval.

Heat integration method

Using this method, the temperatures at all points were observed. For a pure metal, if the temperature at any point exceeds the melting temperature, the material is assumed to have undergone a state transition. The temperature at that point is reset to the melting temperature, and the equivalent amount of heat due to resetting the temperature is added to the enthalpy accounting for that point [111]. Once the accumulation

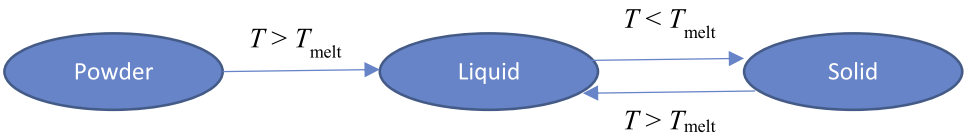

Fig. 12. Three states of feedstock material.

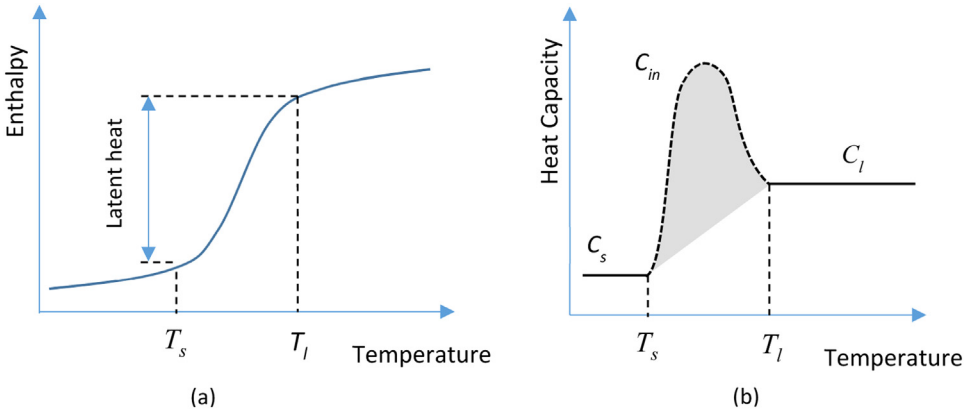

Fig. 13. (a) A typical temperature-enthalpy relationship for non-isothermal state change; (b) Apparent heat capacity method with modified heat capacity C_{in} that includes the effect of latent heat.

was equal to the latent heat, the temperature was allowed to increase. This method is computationally economical, but the accuracy of the solution strongly depends on the size of the time increments [111].

Enthalpy method

In this method, the latent heat is accounted for by enthalpy [111]. The enthalpy as a function of temperature is given by Eq. (6).

$$h = \begin{cases} C_s T & T < T_s, \\ C_m T + \frac{H_f (T - T_s)}{(T_l - T_s)} & T_s \le T \le T_l, \\ C_l\, T + H_f + C_m (T_l - T_s) & T \ge T_l, \end{cases} \tag{6}$$

where C_m is the heat capacity of the material in the mushy zone. Although the enthalpy method is more expensive, it provides accurate solutions [111].

Luo and Zhao [69] performed a transient thermal analysis of a part during the selective laser melting process and adopted the apparent heat capacity method. Foteinopoulos et al. [48] developed a numerical model to simulate the thermal history of parts manufactured using PBF. Changes in the melting and solidification states were modeled using the apparent heat capacity method. Cheng et al. [112] performed a thermal analysis of the PBF process using the enthalpy method to model the latent heat. Parry et al. [113] did not include latent heat in their work to avoid smaller time increments and argued that latent heat is relatively insignificant compared to the loss of heat through radiation. Cheng et al. [112] developed a numerical model in which material properties were assigned according to the state of the material. An internal state variable is defined to specify whether the material is powdered or consolidated. The variable at a material point can be 0 or 1, where 0 represents powder and 1 represents a consolidated state. When the temperature at a material point (in the powder state) exceeded the liquidus temperature, it was considered to have transformed into the consolidated state, and the state variable was changed to 1. Then, the state variable was locked at 1, as the state change could only be one-way (i.e., from powder to consolidated). Similarly, Jeong et al. [114] performed a thermal analysis of the PBF process using temperature-dependent material properties for the powder and consolidated states. They tracked the temperature history of each integration point to determine the state and applied appropriate material properties. The numerical predictions were experimentally validated.

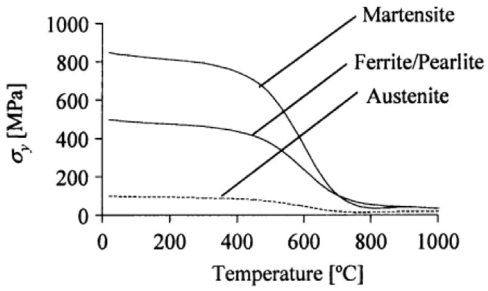

Fig. 14. Dependence of yield limit of martensite, ferrite/pearlite mixture, and austenite on temperature [116].

2.7. Solid-state phase transformations

Solid-state transformations have a significant effect on the physical properties that must be considered to accurately predict the residual stress and strains. The difference in the coefficient of thermal expansion and volume changes due to the difference in the densities of the parent and transformed phases are two of the most important properties to consider in residual stress simulations. Similarly, the different phases exhibit different thermal properties [115]. Furthermore, the mechanical properties of an alloy change significantly due to solid-state transformations because the properties of the individual phases are substantially different from each other. Fig. 14 shows the yield strengths of different phases of a carbon-steel alloy as a function of temperature [116]. Because the yield strengths of each phase are significantly different, it is important to track the phase transformations to accurately model macroscopic alloy behavior.

Materials that do not undergo a solid-state phase transformation, such as Inconel 625 [102], are relatively easier to model. In the case of phase transformation in a material, the total strain is expressed as:

$$\varepsilon^{total} = \varepsilon^{elastic} + \varepsilon^{plastic} + \varepsilon^{thermal} + \varepsilon^{phase}, \tag{7}$$

where ε^{phase} represents the phase transformation strain.

The strain caused by the solid-state phase transformation has been shown to be critical for several materials [102,117]. If the residual stresses are to be predicted accurately, it is necessary to know which transformations are likely to occur because a phase change is usually associated with a transformation strain. It was shown in Ref. [102] that

when transformation strain was not incorporated into the model, the residual stress results were overpredicted by more than 500% for Ti-6Al-4V alloy. This was attributed to the difference in the coefficients of thermal expansion, volume, and hardness between the parent and resulting phases.

The thermal and mechanical fields must be coupled with the evolution of the microstructure to account for the dependence of the physical properties of a material on its microstructure. In the approach adapted by Alberg and Berglund [116], the thermal field is first computed, followed by the microstructural evolution. Finally, the mechanical field is computed.

A numerical model requires separate material models to consider the different constitutive behaviors of each phase present in a part. However, the predictive numerical models for industrial parts would require significant computational resources.

2.8. Material model

Owing to the direct exposure to a heat source, the temperature of a built part can become very high locally. Furthermore, the material undergoes repeated heating and cooling cycles because of pass-by-pass and layer-by-layer movements of the heat source. Due to temperature fluctuations, the behavior of the material changes drastically during the AM process. Therefore, it is important to consider the temperature-dependent properties of materials used in AM [67]. Furthermore, during an AM process, the built part cools rapidly. Typical cooling rates are in the order of 10^5 K/s around the melt pool [50,118]. Such rapid cooling rates can cause significant strain in the surrounding materials. The flow strength of metals usually exhibits significant strain-rate dependence at elevated temperatures [119,120]. Therefore, to accurately model the behavior of materials in an AM process, several authors have considered the material properties over a wide range of temperatures. However, many researchers have used strain-rate-independent material models in their work, probably for ease of implementation and to reduce the computational resources required [50]. Such models cannot directly capture stress and strain relaxation at elevated temperatures.

The solution to the heat conduction equation requires information on the density, heat conductivity, and heat capacity of the material. Generally, it is easier to obtain thermal properties than mechanical properties. Many studies have used temperature-dependent thermal properties for thermal analysis. Hocine et al. [121] developed a FE model to predict the temperature evolution of a part fabricated using the selective laser melting process. They used temperature-dependent thermal properties of bulk materials in their work. The powder density at temperatures below the melting point was obtained by multiplying the bulk density by a scaling factor. The thermal conductivity of the powder was calculated using the following equation: The specific heat capacity was assumed to be equal to that of the bulk material. Zhang et al. [73] developed a heat transfer FE model for the PBF process to predict melt pool dimensions. Temperature-dependent thermal properties of the bulk material were considered. The powder conductivity for temperatures lower than the melting point was assumed to be 1% of the bulk thermal conductivity. The powder density was calculated using the following equation: The specific heat capacity of the powder was assumed to be equal to that of the bulk material.

Constitutive models that describe the response of a material to different loading conditions are required for stress analyses. Accurate prediction of residual stresses requires physically realistic constitutive models, which necessitate a better understanding of the relationship between temperature, microstructure, and material properties. Different constitutive models have been proposed to account for the observed behavior of materials, such as strain dependence, strain rate dependence, temperature dependence, and microstructure dependence. Constitutive models are generally divided into two categories: physics-based and phenomenological. Physics-based models (also known as physically based models in the literature) consider the underlying physical processes, such as dislocation density, recrystallization, grain growth, and grain size gradients, to formulate constitutive equations [122]. In contrast, phenomenological models are based on fitting a function to experimental data without any consideration of the underlying physical process. Several empirical models exist, such as Hollomon's equation and Ludwik's equation, which are power laws used to describe the hardening behavior of metals. A commonly used model for strain-rate-dependent materials is the Johnson-Cook (JC) model. Such models are not based on the knowledge of the underlying deformation mechanism. These models generally exhibit a good fit to the measured stress–strain curves. However, they have no predictive capability beyond the range of the measured data. Hence, they usually provide good results within the range of conditions in which they are fitted, and the accuracy outside that range is often unsatisfactory. However, physics-based models can be extrapolated outside the range of data used for calibration, provided that the underlying mechanisms still dominate the behavior [123]. Therefore, it provides a more realistic prediction than phenomenological models. A phenomenological model has fewer parameters to fit than a physics-based model.

Yang et al. [97] predicted residual strains within an Inconel 625 part using a sequentially coupled thermomechanical model. A temperature-independent material model of Inconel 625 was used for mechanical simulation. A bilinear orthotropic plasticity-hardening behavior was implemented in this model. Different yield strengths are assumed in the horizontal and build directions. The material model is justified based on the accuracy of the predictions. Dong et al. [124] modeled the mechanical behavior of a material as an ideal plastic using the von Mises yield criterion to predict the residual stresses in a part built using the PBF process. Song et al. [125] implemented a temperature-dependent plasticity model using the von Mises yield criterion to investigate the process of simulation of AM components fabricated using Inconel 718. As the previously deposited material undergoes remelting and heating cycles owing to the new material deposition, it is supposed to undergo annealing. The process of annealing (heat treatment) involves maintaining a suitable temperature, which is significantly lower than the melting temperature, for a certain amount of time (usually hours) for microstructural changes to occur. However, the temperatures increase locally for only a very short period during the AM of a part. Therefore, annealing is anticipated to occur only in regions where the temperatures are significantly higher than the published full annealing (heat treatment) temperatures [126,127]. However, annealing data for higher temperatures are scarce, so in Ref. [126], an annealing temperature of 1200 °C was assumed for welding of steel, keeping in view shorter exposure times. Several studies [102,113,128,129] have modeled annealing by resetting the strain components to zero above a certain reference temperature. The value of the reference temperature usually needs to be tuned to best match the experimental results. To capture the annealing phenomenon, Qiao et al. [127] adopted the dynamic strain-hardening reduction factor.

When this factor was set to 1, the dislocations were completely annihilated, such that all strain hardening effects were eliminated, and the material returned to a fully annealed state without any dislocations. In contrast, when this factor was set to zero, there was no dislocation annihilation. (e.g., when deformation was complete at room temperature). It was also shown that this reduction factor was more sensitive to temperature than to time. Ganeriwala et al. [50] combined three different classes of material models to capture the strain-rate dependence and annealing behavior of Ti-6Al-4V. The adopted model depends on the temperature as follows:

(1) Strain rate independent plasticity for $T < 0.5T_m$;
(2) Viscoplasticity (strain rate dependent plasticity) for $0.5T_m \leq T < 0.8\ T_m$;
(3) Maxwell-type viscoelasticity for $T \geq 0.8\ T_m$.

Where T_m is the melting temperature of the material and T is the temperature at a given point. The results of the thermomechanical simulation were in good agreement with the synchrotron X-ray diffraction

measurements. Lindgren et al. [130] developed a physics-based flow stress model for Ti-6Al-4V. This model allows the removal of accumulated plastic strains corresponding to the annealing of the material. They coupled a constitutive model with a microstructural model. Urevc et al. [131] implemented a phenomenological viscous-elastic-plastic constitutive model to simulate the stress relief in AISI 316 L austenitic stainless steel. Zhao et al. [132] compared the Johnson-Cook and modified Johnson-Cook constitutive material models to predict the behavior of FeCr alloys during AM. The dynamic impact tests were conducted at various strain rates and temperatures. Gupta et al. [133] developed four constitutive models to predict the flow stress in 316 austenitic stainless steels. They concluded that the modified Zerilli-Armstrong and Arrhenius models predicted the flow stress better than the Johnson-Cook model. Promoppatum and Rollett [122] compared physics-based (Mechanical Threshold Stress) and phenomenological (Johnson-Cook) models for thermomechanical simulations. The results showed that the mechanical threshold stress model has an advantage in capturing the transient growth of plastic strain compared with the Johnson-Cook model.

2.9. Scanning strategy

Scanning strategy refers to a pattern in which the heat source moves over a substrate. These components can be fabricated using different scanning strategies. Several aspects and parameters are associated with the scanning strategy. These include the scan vector length, angle of the scan vectors, order of scanning, and rotation of the scan vector during the construction of subsequent layers [41,134]. Varying any of these can result in significant combinations of the scanning strategies. Various scanning strategies have been implemented and described in literature. The basic strategies described in the literature are shown in Fig. 15.

The choice of scanning strategy significantly affects residual stress and distortion [11,38–41]. Moreover, scanning strategies determine several other characteristics of the built part, such as the mechanical properties, density, and surface finish. The scanning strategy affects the thermal history, which consequently affects the solidification pattern. Consequently, components with similar geometries built using different scanning strategies can exhibit completely different physical properties [40,135].

Scanning strategies for PBF process

Kruth et al. [136] investigated the effects of different scanning strategies on the deformation of a part fabricated using the laser-PBF process. They observed that sector-wise scanning resulted in smaller deformations than unidirectional scanning. Ali et al. [134] investigated the effect of the scanning strategy on residual stress development during the laser PBF process. They reported that a 90° alternating scanning strategy, in which the orientation of each new layer was rotated by 90°, resulted in the lowest residual stress. An FE model with a moving volumetric heat source was developed to understand the effect of the scan vector length on temperature evolution in the powder bed. Parry et al. [113] implemented a fully coupled thermomechanical model to simulate PBF. The deposition of a single powder layer on a substrate was simulated using a volumetric Gaussian heat source. The results showed that stress was generated as consolidated material behind the cooled and contracted melt pool. Furthermore, the longitudinal stress (i.e., along the scan vector) was higher than the transverse stress. This was attributed to the higher temperature gradient along the scan vector than perpendicular to it, and to the lack of solid material inhibiting thermal expansion in the perpendicular direction. It was also observed that the longitudinal stress increased with the scan vector length. Robinson et al. [137] experimentally studied the influence of seven different scanning strategies on residual stresses in PBF-built parts. The stress distribution along the thickness of each part was estimated using the contour method. The results showed that the part built using the *XY* alternating strategy, in which scan vectors alternate along the x- and y-axes on consecutive layers, yielded the lowest measured residual stress. Kruth et al. [138] experimentally studied the effect of the scanning vector length and scanning pattern on the residual deformation in a laser PBF-fabricated component. The residual deformation exhibited a decreasing trend when the scan vector length was reduced. Furthermore, the island scanning pattern reduced the residual deformation, and the minimum deformation was observed when the scanning path was inclined 45° to the x-axis. Cheng et al. [101] developed a sequentially coupled thermomechanical model to test various scanning strategies for PBF. Three layers of powder and a conical moving heat source were considered for the simulation, without any agglomeration technique. Owing to the high computational costs, only a small scanning domain of 6 mm × 6 mm was considered. The results revealed the effects of different scanning strategies on temperature, stress, and deformation. However, no physical experiments have been conducted to validate these results. It was shown that the 45° inclined back-and-forth line scanning caused the lowest residual stresses. Ganeriwala et al. [50] investigated the strain field using a thermomechanical model, while adopting layer and heat source agglomeration. Bridge-shaped specimens were produced by the PBF process using different scan strategies, and the residual strain fields were measured using synchrotron X-ray diffraction. The measurements showed different strain distributions in the parts depending on the scan strategy. The simulation results were unable to capture all scan strategy effects correctly. They concluded that scan strategy effects could not be captured when agglomeration techniques were used.

Scanning strategies for DED process

Many studies have been conducted to investigate the effect of the scanning strategy on the residual stresses in parts produced by PBF. However, only a limited number of studies have investigated this phenomenon during DED [139]. DED is quite different from the PBF process, for example, in terms of the power and moving speed of the heat source, layer thickness, and bead profile size. Therefore, applying the conclusions drawn from PBF-related studies to DED is not straightforward. Yu et al. [140] applied four different deposition patterns to construct parts. They compared the distortions of the parts and determined that the fractal deposition pattern yielded the lowest distortion. They also developed a finite element model to perform a thermal analysis of the build process and concluded that the magnitude of the temperature gradient has a critical effect on part distortion. Yan et al. [141] compared an island scanning pattern and an interlayer orthogonal reciprocating scanning pattern to determine their influence on substrate distortion and residual stress distribution for large DED-built parts. The results showed that the island scanning pattern reduced distortion by 71%. Furthermore, the island scanning order had a more significant influence than the island size on the deformation and residual stress. Saboori et al. [142] produced cubes by DED using two different deposition strategies: 0°~90°, which is an orthogonal rotation between two layers, and 0°~67°, which is a 67° rotation for each new layer. They observed higher residual stress values on the lateral surfaces of cubes produced using the 90° deposition strategy. Wang et al. [143] developed a thermomechanical finite element model to simulate the effects of scanning strategies on the residual stress and deformation of components using a high-power DED process. The results showed that different heat source jump strategies between the islands resulted in substantial differences in residual deformation. The increase in the heat-source jump distance between the islands resulted in residual deformation reduction. The results also showed that the residual stress and deformation decreased with decreasing island size. Zhou et al. [144] investigated the planning of a continuous tool path for a wire-arc AM process with the aim of reducing the residual stress. In the wire-arc process, a continuous toolpath is typically preferred because of the better surface quality and forming efficiency of the part compared with a discontinuous toolpath. However, a continuous toolpath can result in an uneven thermal distribution and higher residual stress. Zhou et al. used an evolutionary method based on a genetic algorithm to plan a continuous tool path. The experiments showed that the optimized toolpath obtained using the proposed method yielded a smaller magnitude

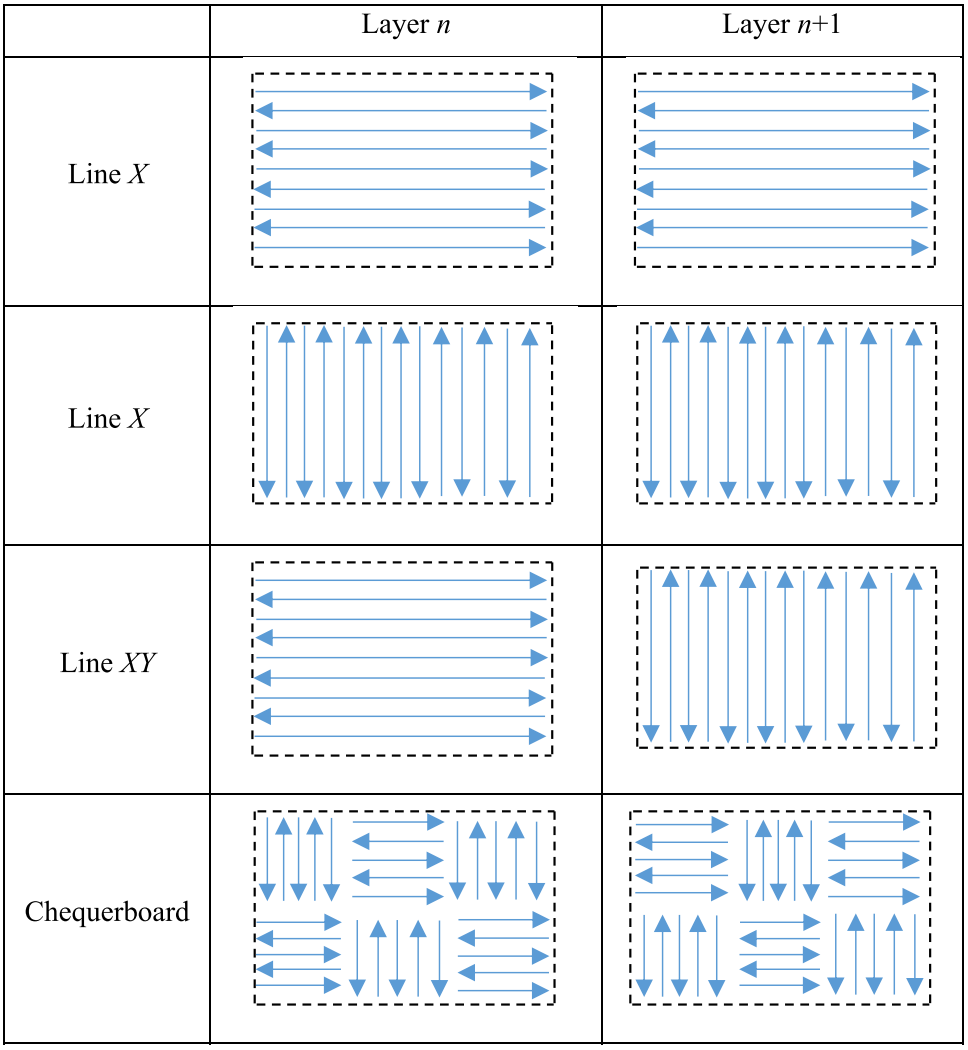

Fig. 15. Schematic of four different scanning strategies.

of residual stress and distortion than the initial toolpaths. Aliyev et al. [145] investigated the effects of different deposition strategies on the thermomechanical characteristics of the Inconel 718 deposited region on a cantilever substrate using a laser-engineered net shaping process. They concluded that the zigzag deposition strategy performed better than the unidirectional deposition strategy, because the distortion of the former during the deposition and cooling stages was significantly smaller.

In addition to the scanning strategy, the inter-layer dwell time also affects the microstructures of additively manufactured parts. The inter-layer dwell can be defined as the time between the completion of the current layer and the beginning of the next. Denlinger and Michaleris [102] showed that Inconel 625 exhibited increasing distortion with decreasing dwell time; however, the distortion dramatically decreased with decreasing dwell time for Ti-6Al-4V. By simulating this problem, they explained that reducing the dwell time resulted in higher temperatures in the build as the cooling duration was reduced, which resulted in higher distortion and residual stress in the Inconel 625 part. Similarly, shorter dwell times in Ti-6Al-4V builds resulted in higher in-process temperatures, but higher temperatures promoted phase transformation. This causes considerable transformation strain, which opposes all other strain components [135]. The offsetting of strains owing to thermal contraction by transformation strains changes the residual stress distribution. Consequently, lower levels of distortion and residual stress were observed. Because Inconel 625 did not undergo a solid-state phase transformation, stress relaxation was not observed. After including the transformation strain in the constitutive model, numerical simulations provided predictions that agreed well with the experimental results.

The choice of the scanning strategy is critical for addressing the residual stress and distortion in AM-built components. By effectively integrating the scan strategies, hatch length, hatch spacing, dwell time, and scan speed during the preprocessing stage, residual stress effects can be mitigated [41]. Furthermore, new strategies need to be devised to reduce stress levels and avoid time-consuming and costly post-processing steps.

Important models

High-fidelity models have been used by many researchers to simulate the residual stress and strain in AM-built parts. Yang et al. [88] developed a sequentially coupled thermomechanical model to predict the thermomechanical behavior of a DED-built component. An ellipsoidal heat source model was employed. To validate the thermal-analysis results, two thermocouples were attached to the substrates. It was concluded that both the measured and simulated temperature histories followed the same trends, although there was a discrepancy in magnitude. Furthermore, the computed deformations agree well with the measured deformations. Ganeriwala et al. [50] used layer and heat-source agglomeration to simulate the residual stress and strain in a bridge-shaped component. They used a fully coupled thermomechanical model for the analysis. The heat source was modeled as a uniformly distributed volumetric model to improve the computational performance. A material model was developed to capture the strain rate dependence and annealing behavior at higher temperatures. Comparisons between the strains simu-

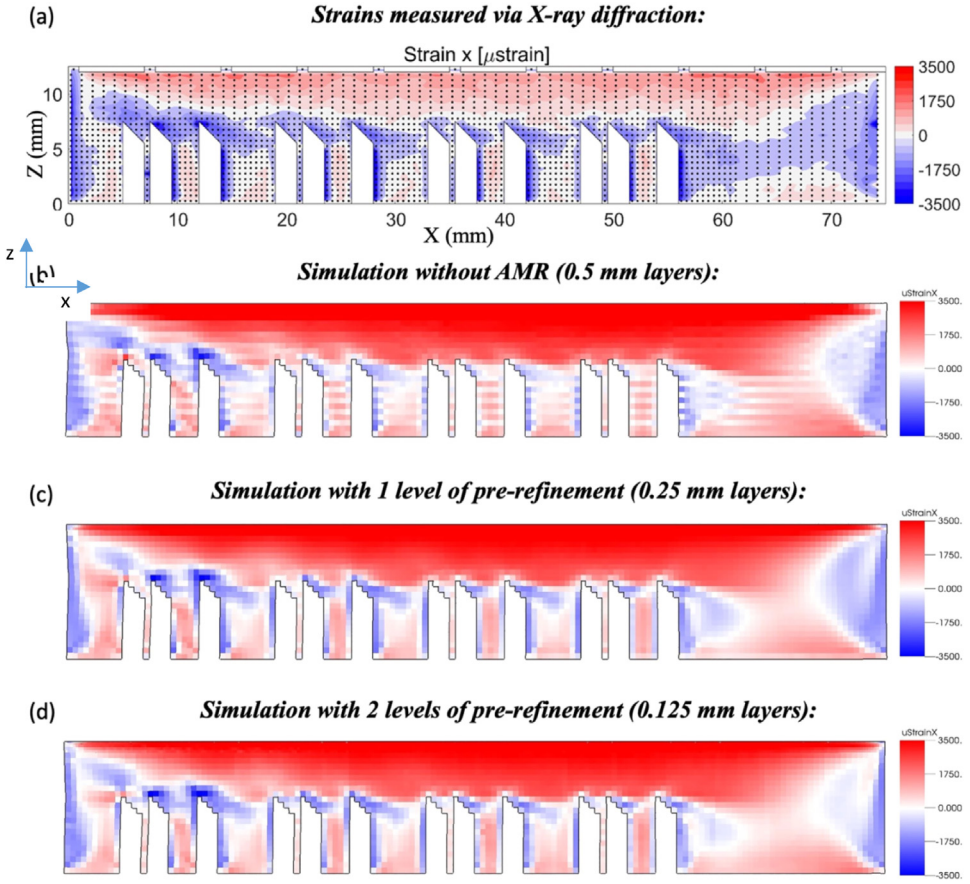

Fig. 16. Contour plot of residual strain in the *x*-direction in the middle plane of the bridge structure: (a) Measured using X-ray diffraction; (b) Simulated without AMR with a layer height of 0.5 mm; (c) Simulated using 1 level of pre-refinement; (d) Simulated using 2 levels of pre-refinement [98].

lated and measured using X-ray diffraction showed good qualitative and quantitative agreement. Chen and Yan [146] used a high-fidelity modeling approach to simulate thermal stress. Instead of using a heat source model, they used the temperature profiles obtained from the thermal fluid model as a load. Thermal loads were applied using a linear interpolation function to map the temperature values from the cell centers of the thermal fluid model into element nodes in the FE model. Because of the extensive computational resources required, they used this approach only to simulate the thermal stress evolution in a few tracks and layer depositions. However, they planned to efficiently simulate the entire part by adopting a multiscale modeling approach in the future. Yang et al. [97] used sequentially coupled thermomechanical analysis to simulate the residual strains in a bridge-shaped laser PBF-built specimen. The laser was modeled as a moving concentrated point heat source during the thermal analysis. A layer-lumping technique was used to reduce the DoF. The thermal history was imported into the mechanical model as a predefined field. The predicted results were compared with X-ray diffraction measurements, and a good level of agreement was observed. Ganeriwala et al. [98] used layer and heat source agglomeration in a fully coupled thermomechanical analysis to simulate residual strains in the same bridge-shaped specimen, as considered in the work by Yang et al. [97]. They used a layer-wise AMR technique to reduce the DoFs. The elements in the current layer were not refined/de-refined as a function of the laser position; instead, the elements in the previous layers de-refined as new layers were added. The de-refinement was based on the distance from the top surface of the part. By comparing the predicted results with X-ray and neutron diffraction measurements, they concluded that the simulations captured the general trend; however, in some areas, the residual strains were overpredicted. Fig. 16 shows a comparison of the measured and simulated results in the longitudinal direction with and without AMR.

Final comments

High-fidelity models require spatial discretization of an order smaller than the melt pool size. They also require temporal discretization, which corresponds to the scanning speed of the energy source, to accurately capture the local stress and temperature fields [147]. Owing to the tremendous computational resource requirements, high-fidelity models have mostly been used for parts of limited size and complexity. The fundamental challenges in this approach are the number of time increments required to prevent aliasing and the fine mesh. Despite the availability of powerful computers in recent years and the aforementioned techniques for reducing the DoF, high-fidelity models are mostly limited to modestly sized models [107].

3. Simplified Models

High-fidelity models have been used by several researchers for AM process simulation [50,97,104]. The predicted results in these studies were validated by comparing them with measurements. However, high-fidelity models require significant computational resources, making their use on an industrial scale impractical. To make the modeling process time efficient, drastic assumptions were made to develop simplified models (also called reduced-order models [148]). Usually, a complete layer is assumed to be deposited simultaneously and subjected to a uniform load, for example, heat flux, strain, or temperature field, instead of being scanned using a moving heat source. Layer lumping was also implemented in the simplified models, further reducing the computational cost.

Several simplified approaches have been developed to model part-scale behavior to obtain results quickly. The simplified models yield quicker results at the cost of accuracy loss. One of the most promising and simplified approaches is the inherent-strain method [149]. The application of plastic strain [150] is another simplified method inspired by the inherent strain method. In another method (referred to as the

flash heating method in this paper), a uniform heat flux is applied to a complete layer or a fraction of the layer, and the thermomechanical problem is solved [151,152]. In a variation of the flash heating method, a uniform temperature field, instead of a heat flux, is applied as a load to the complete layer to simulate the AM process [100,153].

Owing to their popularity, inherent strain and thermomechanical macrolayer methods are described in the following sections.

3.1. Inherent strain method

The inherent strain method is an inexpensive method that enables fast prediction of the mechanical histories of built components. It simulates part-level behavior by performing a mechanical analysis instead of a computationally expensive thermomechanical analysis. The layer is assumed to be instantaneously deposited. The deformation of the material in a layer is induced by specifying the strain tensor as the initial load, and the equilibrium solution is sequentially computed for each layer.

The fusion zone created after scanning the power source experiences an almost identical thermomechanical history for the complete part. This hypothesis was used to reduce the expensive thermomechanical problem to a significantly less demanding problem [154]. Therefore, for a particular material under a certain set of process parameters, an inherent strain tensor is determined, which is assumed to be the same for any other part built using the same material and process parameters. This inherent strain tensor was used to compute the residual stress and deformation in an AM part by performing a mechanical analysis instead of simulating the problem using a thermomechanical model. The mechanical behavior of the welded structures was simulated by adopting linear-elastic material models for the inherent strain method. However, such models are insufficient for parts fabricated using AM; instead, elastoplastic material models have been implemented [53,94].

Consider the bar shown in Fig. 2. When the bar is cooled, the thermal strain becomes zero, and only the residual elastic and plastic strains exist. According to the inherent strain theory, if the final plastic strain in the bar is known, it is possible to compute the elastic strain, and hence the residual stress, without knowing the thermal history. This has been used to compute residual stresses in welded structures using the inherent strain method [149].

During the welding or AM process, the total strain is divided into elastic, plastic, thermal, creep, and strain induced by phase transformation, which is expressed as:

$$\boldsymbol{\varepsilon}^{total} = \boldsymbol{\varepsilon}^{elastic} + \boldsymbol{\varepsilon}^{plastic} + \boldsymbol{\varepsilon}^{thermal} + \boldsymbol{\varepsilon}^{creep} + \boldsymbol{\varepsilon}^{phase}, \tag{8}$$

where $\boldsymbol{\varepsilon}^{creep}$ and $\boldsymbol{\varepsilon}^{phase}$ represent the creep and phase transformation strains, respectively. The inherent strain is defined as the sum of all strains other than the elastic strain and is expressed as:

$$\boldsymbol{\varepsilon}^{inh} = \boldsymbol{\varepsilon}^{total} - \boldsymbol{\varepsilon}^{elastic} = \boldsymbol{\varepsilon}^{plastic} + \boldsymbol{\varepsilon}^{thermal} + \boldsymbol{\varepsilon}^{creep} + \boldsymbol{\varepsilon}^{phase}. \tag{9}$$

Once the inherent strain is determined, it is introduced into the FE model as the initial strain [155,156]. The equivalent nodal load is computed using the following relation:

$$\boldsymbol{f} = \int \boldsymbol{B}^{\mathrm{T}} \boldsymbol{D} \boldsymbol{\varepsilon}^{inh} \mathrm{d}v, \tag{10}$$

where $\boldsymbol{B}$ is the strain-displacement matrix, and $\boldsymbol{D}$ is the elastic stress–strain matrix. The nodal load is then used to compute the nodal displacement using the following relationship:

$$\boldsymbol{u} = \boldsymbol{K}^{-1} \boldsymbol{f}, \tag{11}$$

where $\boldsymbol{K}$ denotes the stiffness matrix. After the nodal displacement is obtained, the total strain can be computed using the following relation:

$$\boldsymbol{\varepsilon}^{\mathrm{total}} = \boldsymbol{B}\boldsymbol{u}. \tag{12}$$

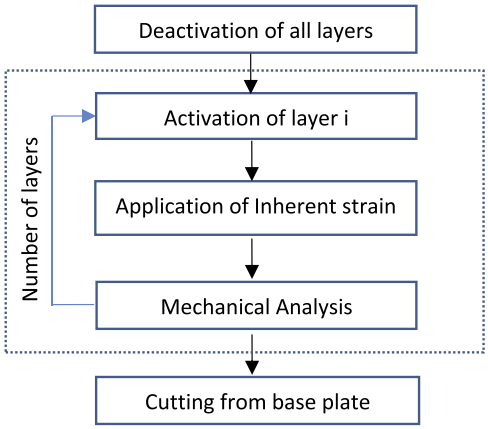

Fig. 17. Schematic workflow of the inherent strain method [157].

Stresses can be computed using Hooke's law as:

$$\boldsymbol{\sigma} = \boldsymbol{D}\boldsymbol{\varepsilon}^{elastic} = \boldsymbol{D}\left(\boldsymbol{\varepsilon}^{total} - \boldsymbol{\varepsilon}^{inh}\right). \tag{13}$$

In the framework of the inherent strain method, the fabrication of an AM part is approximated using layer-by-layer material deposition. Hence, the geometry of the built component is discretized into layers. At the beginning of the analysis, all the layers are deactivated. At each time step, a new layer is activated, and the inherent strain tensor is applied as an initial load to all the elements in that layer. Therefore, the elements in a layer are not a part of the model until the layer is activated, resulting in smaller FE models. The process of layer activation and inherent strain application was repeated until all the layers were added to the model. Finally, the cutting of the built part from the base plate was modeled using deactivating elements. Temperature-independent material properties were used in this analysis. The workflow of this method is schematically shown in Fig. 17. Note that a temperature history is not required, and only the mechanical problem is solved. The layer activation strategy for the intermediate state of the simulation is schematically shown in Fig. 18. In this figure, the current layer is the layer activated in the current step for inherent strain application. It is also a common practice to combine several physical layers into a single computational layer [157]. In the literature, a part-level model is also known as a macroscale model.

Computing inherent strain

One of the main challenges in the inherent strain method is the estimation of the inherent strains. The following two methods are available in the literature for estimating the inherent strain:

(a) Empirical method;
(b) Meso-scale submodel.

The empirical method involves fabricating a test part using AM and measuring the distortion after cutting the part from the build plate. An inverse analysis is then performed using a mechanical FE model to determine the inherent strains of the test part [157]. The inverse analysis involves specifying a range of inherent strain values that can contain inherent strains for the test part. Subsequently, a few sample points are set, and finite element analysis is performed to calculate the distortion. An error function is defined by comparing the computed and measured distortions. Inverse analysis aims to minimize the error and search for an accurate value of inherent strain, such that the computed distortion becomes equal to the measured distortion [158].

Siewert et al. [159] built a twin-cantilever beam and determined its inherent strain using an empirical method. They used Newton's method to minimize the error and determine the optimum, that is, the inherent strains that reduce the difference between the measured and computed

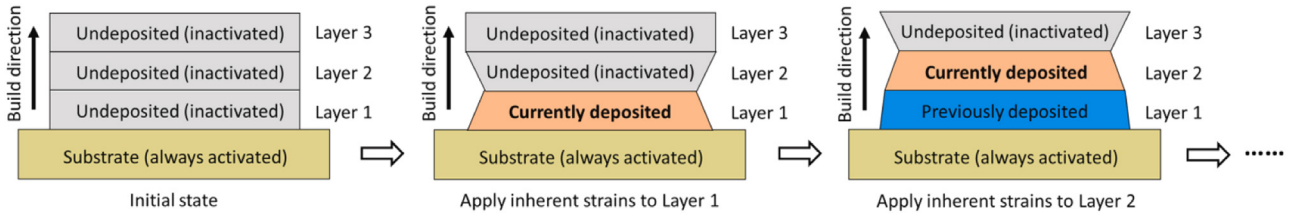

Fig. 18. Analysis workflow for the inherent strain method for part-scale simulation (The current layer is the layer that is activated in the current step for inherent strain application [124]).

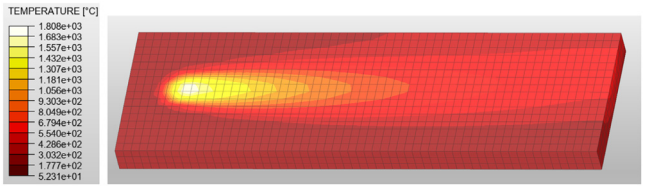

Fig. 19. Simulation of the building of a specimen to determine the inherent strain tensor using AdditiveLab [160].

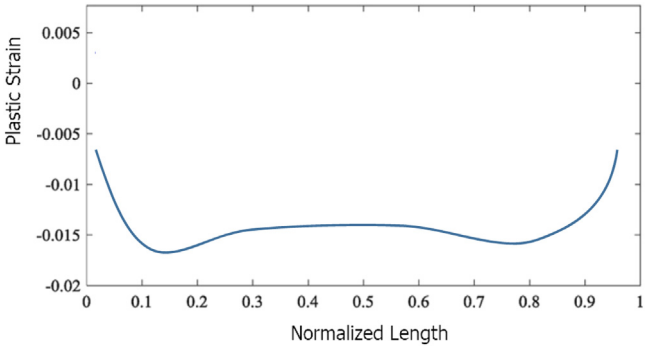

Fig. 20. Schematic plot of the plastic strain in the bottom layer along a path defined in the middle of the representative volume.

distortions to zero. The calibrated strains were used to simulate another part built using the same processing parameters as those used for the twin-cantilever beam. The difference between the measured and computed distortions in this part was negligible. Setien et al. [157] built a twin-cantilever beam and calibrated the inherent strains using an empirical method. The Hooke-Jeeves direct penalty technique was used to solve the optimization problem and minimize errors. They built several beams using different scanning strategies and concluded that periodic scanning strategies resulted in-plane isotropic inherent strains. Chen et al. [158] built a two-layer structure on a substrate using DED. The substrate was clamped to only one side. The measured distortion of the substrate was used to compute inherent strains. A multifactor uniform experimental design was used to establish sample points for the FE simulation, and a genetic algorithm was used to solve the optimization problem. It was found that the average error was less than 6% while using the computed inherent strains to simulate the distortion in AM parts.

The mesoscale submodel (also called the microscale submodel in some studies [53]) is a numerical technique for determining the inherent strain tensor with little or no dependency on physical tests [53,157]. This involves the simulation of the building process of a small component, usually called a representative volume, using a sequentially coupled thermomechanical analysis. This includes a transient thermal analysis, followed by a static stress analysis. The temperature history for all elements from the thermal analysis was introduced as the initial load during the stress analysis. Temperature-dependent material properties are required for the analysis. The inherent strain tensor components are extracted when the part is cooled to the ambient temperature. The build simulation was conducted by considering the scanning strategy and process parameters used for the fabrication of the actual part. Fig. 19 shows a simulation of such a specimen for a powder-bed fusion process with a laser of diameter 0.1 mm [162]. Each layer is scanned using five trajectories in alternating directions.

An important consideration when defining a mesoscale model is the number of layers required for the inherent strain extraction. This usually depends on the thickness of the feedstock material and the depth to which the heat source affects the magnitude of the plastic strain. It is usually sufficient to simulate a three-layer model for inherent strain extraction in a laser PBF (LPBF) process [28]. However, for a directed energy deposition (DED) process, it is sufficient to have a two-layer model because of the much thicker deposition layer compared to the LPBF process [28].

After the simulation results were obtained, the final plastic strain state of the representative volume was plotted. The plastic strain tensor consists of shear and normal components. The shear strain components have considerably smaller magnitudes and are therefore ignored. Only the normal strain components are considered for the inherent strain definition [94,154]. Two methods are used to extract the inherent strain tensors. Fig. 20 shows a schematic of the residual plastic strain in the build plane of the first layer of the representative volume. Chen et al. [53] considered steady-state values in the middle region of the plot for the inherent strain tensor. In contrast, Bugatti and Semeraro [94] computed a weighted average of the strain components using their centroid values and element volume as the weights for all elements in the build plane. The weighted average values were used to define the inherent strain tensor.

The inherent strain method is a multiscale process modeling framework. A mesoscale model is used to determine the inherent strain tensor. Subsequently, a macroscale FE model was developed to determine the residual stress and strain distributions in the actual part. Temperature-independent material properties were used during macroscale mechanical analyses, resulting in simpler models. The computational resources required for macroscale mechanical analysis were significantly lower than those required for thermomechanical analysis. Once the inherent strain tensor for a particular material and processing parameters are obtained, a part-level layer-by-layer analysis can be performed directly without repeating the analysis using the mesoscale submodel if the processing conditions are the same. Therefore, a reference database could be constructed for different materials using different process parameters and scanning strategies. Fig. 21 schematically shows the workflow of the multiscale process modeling framework based on the inherent strain method used to model the AM.

The predictions made using the inherent strain method for the metal welding process were validated by experimental results [28]. However, the inherent strain method does not provide satisfactory results for AM. This is attributed to the fundamental differences between welding and AM processes. To address this issue, a modified definition of inherent strain has been proposed [28].

Modified inherent strain method

The original inherent strain method assumes that the residual elastic strain is either insignificant compared with the residual plastic strain or

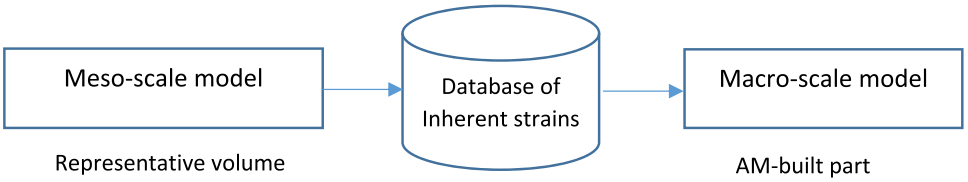

Fig. 21. Workflow of the multiscale process modeling framework based on the inherent strain method.

is relaxed because the welded parts are not fully constrained [28,53]. Hence, the computed plastic strain was directly applied as the initial strain in the part-scale model. However, the elastic strain does not relax when the part cools to the ambient temperature in AM. Furthermore, owing to changes in the magnitude of the accumulated plastic strain caused by repeated heating and cooling, the stress–strain history must be considered to correctly determine the present state of the material. A modified inherent strain (MIS) model was proposed to account for the differences in both processes. The modified inherent strain is defined as the difference between the total mechanical strain at the intermediate state and the elastic strain at the steady state, and can be expressed as [28,53]:

$$\boldsymbol{\varepsilon}^{inh} = \boldsymbol{\varepsilon}_{t_1}^{plastic} + \boldsymbol{\varepsilon}_{t_1}^{elastic} - \boldsymbol{\varepsilon}_{t_2}^{elastic}, \tag{14}$$

where t_1 is the intermediate state when the power source passes and the compressive mechanical strain reaches its peak magnitude, and t_2 is the steady state when the deposited part cools to the ambient temperature.

After extraction of the inherent strain vector, a mechanical analysis was performed using a macroscale model in which temperature-independent material properties were used.

Limitations of the modified inherent strain method

Several studies have validated the results obtained using the MIS method by comparing the residual deformation of the built part after being cut from the base plate [28,53]. However, detailed comparisons of the distributions of residual stresses and strains are lacking. Dong et al. [124] showed that the MIS method provided an inaccurate residual stress prediction. They proposed a new implementation procedure to improve the simulation accuracy of the residual stress. In this procedure, inherent strains were applied using the material properties at an intermediate-state temperature. After solving for equilibrium, the material properties of the current layer were changed to those at steady-state temperature. The equilibrium was resolved again, while maintaining the same inherent strains. Experimental validation using as-built PBF parts showed a significant improvement in the accuracy of the residual-stress prediction without affecting distortion prediction.

The fundamental hypothesis of the inherent strain method is that the inherent strain depends only on the thermal history and is not a function of the geometry or dimensional characteristics of the part [94]. Another assumption of the inherent strain method is that each layer is subjected to a uniform temperature history. Therefore, each layer in the model was subjected to the same inherent strains [53,94]. However, owing to the varying thicknesses of a part's geometry and the varying heat conduction to the base plate during the building of a layer, the material cools at different rates, resulting in temperature gradients in different directions. Consequently, a layer may not be subjected to a uniform temperature history. Furthermore, layers at different heights may experience varying thermal histories [53]. Therefore, the permanent strain accumulated during the building process could be different in each layer and might possess different mechanical properties owing to the different microstructures. To improve the prediction accuracy, the effect of varying the thermal history on the inherent strain tensor should be considered. This is particularly important for large parts built using AM.

The MIS method generally yields good results for the PBF and DED processes with relatively small parts. However, for large parts, the predicted results do not agree well with the measurements [161]. To address this, Dong et al. [161] implemented a temperature-dependent MIS method. In this implementation, each layer was divided into several segments and temperature-dependent inherent strains were applied to each segment according to the temperature of the material in the segment. A mesoscale model was used with different parameters to develop the inherent strain-versus-temperature relationship. Compared with the constant MIS method, the maximum distortion error was reduced from 29.7 % to 7.9 % for a large wall using the temperature-dependent MIS method.

Many parts built using AM require support structures for successful building processes. Cellular lattices have recently been used as support structures. While simulating the residual stress and distortion, the geometry of the support structure must be considered alongside the component geometry for accurate prediction. However, the inclusion of complex lattice support structures increases the required computational resources. Liang et al. [162] proposed an inherent strain method based on homogenization to address this problem. Using homogenization, thin-walled lattice structures can be treated as solid continua. This results in a significant improvement in the computational performance. The results showed that using homogenization, a 10 times speedup can be achieved compared to the case when homogenization is not used.

Noll et al. [163] developed a phase transformation model and implemented it within the framework of the inherent strain method to consider phase transformations in AM-built parts. First, a single-melt-line simulation was performed using a phase transformation model with a Goldak heat source. The results from the single-line simulation were used in the layer-hatch model, from which the inherent strains were extracted. A simplified constitutive model was used for the layer-hatch model. The aim of the single-melt line simulations was to calibrate the heat source model on a realistic material model such that the melt pool geometry correlated with observations in the physical experiments. The results showed that the melt-line simulations could adequately predict different melt-pool geometries. However, they did not simulate the residual stress and deformation in a part model using the framework and left it for future work. In their subsequent work [164], Noll et al. used the extracted inherent strains to investigate the residual stress and strain in a twin cantilever beam built using a laser PBF process. In most studies on the inherent strain method, the shear components of the inherent strain tensor are neglected because of their very small magnitudes. However, Noll et al. reported large shear components and did not ignore them.

Shiyan and Achuthan [147] developed a hybrid model in which they used both high-fidelity and inherent strain methods within a single part to simulate residual stress and strain. They divided the parts into two regions depending on the stress gradient level. Higher stress gradient regions were simulated using the high-fidelity method and lower stress gradient regions were simulated using the inherent strain method. For the bracket like part, the computational savings were approximately 44% using the hybrid approach compared with the high-fidelity method.

3.2. *Flash heating method*

In this method, the deposition of material is assumed to occur simultaneously as an entire layer, and a uniform heat flux is specified as the load for the entire layer [52,151,152,165]. Coupled thermomechanical analysis was performed to determine the temperature and deformation histories. Later, the part was allowed to cool, and a new layer was de-

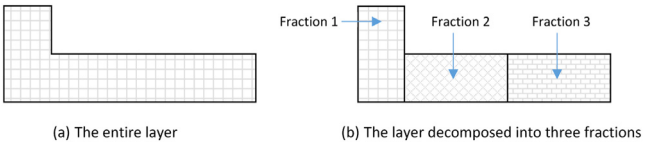

Fig. 22. Decomposition of a layer into fractions to be heated consecutively [151].

posited. In this way, the simulation of the fabrication process progressed layer-by-layer. This method was further developed by Zhang et al. [151], such that each layer could be decomposed into several layer fractions, as shown in Fig. 22. When a layer consists of multiple fractions, the entire fraction of the layer is assumed to be deposited simultaneously and the remaining fractions are assumed to be deposited successively. When a layer is divided into multiple fractions, it is called the sequential flash heating (SFH) method [166].

Each layer or fraction, if the layer consists of multiple fractions, is exposed to heat energy for a t_{heat} time interval, as estimated by the following relation:

$$t_{heat} = \frac{\varphi_L}{v_L}, \tag{15}$$

where φ_L is the laser beam diameter and v_L is the laser scanning velocity. Note that the time interval is not specific to a layer; that is, its value is the same, irrespective of the size of the layer or fraction. After heating, the layer and built part are allowed to cool for t^{lf}_{cool} interval, which is given by Eq. (16).

$$t^{lf}_{cool} = t^{lf}_{scan} - t_{heat}, \tag{16}$$

where t^{lf}_{scan} is the actual scan time of a layer fraction. Fig. 23(a) describes the heating and cooling sequences of the layer fraction. Fig. 23(b) shows the successive treatments of the layer fractions over time.

A uniform heat flux was applied during the heating interval along the surface of the layer. The total energy input during the scanning of a layer fraction can be expressed as Eq. (17).

$$(1 - R)P_L t^{lf}_{scan}, \tag{17}$$

where R is the reflection coefficient of the laser radiation at the surface and P_L is the nominal laser power. The energy balance equation can be written by considering the surface heat flux $\dot{q}_L$, which should be applied to the surface area S^{lf} of the layer fraction during the heating time t_{heat}:

$$(1 - R)P_L t^{lf}_{scan} = S^{lf}\dot{q}_L t_{heat}. \tag{18}$$

The heat input was uniformly applied to the entire thickness z^{lf} of the layer fraction using a volume heat source $\dot{Q}_L$. This uniform volume source is then given by Eq. (19).

$$\dot{Q}_L = \frac{\dot{q}_L}{z^{lf}} = \frac{(1 - R)P_L t^{lf}_{scan}}{S^{lf} z^{lf} t_{heat}}. \tag{19}$$

After sequentially simulating all fractions of a layer, an inter-layer dwell time is required, which corresponds to the spread of a new powder layer and movement of the roller at the top surface of the recently added layer.

Bayat et al. [166] used this method to simulate residual distortion in PBF-built parts. The results showed that when a complete layer was activated simultaneously, the results were insensitive to the scanning pattern and the distortion was overestimated. Furthermore, if the SFH is used, the predicted distortion approaches the experimental measurements as the fraction size is refined. However, this results in increased computational time. Santi et al. [148] used SFH to simulate the residual strains and deformations in a PBF-built bridge-like structure. They reported a good agreement between the strains measured using X-ray diffraction and the predicted strains in terms of both magnitude and spatial distribution. Ganeriwala et al. [50] used FH to simulate residual strains in a PBF-built part and compared the results to a high-fidelity simulation in which a layer and heat source agglomeration were used. They concluded that the results were very similar; however, the FH simulation was significantly cheaper computationally.

As a variation of the SFH method, Williams et al. [100] applied a uniform temperature as the load instead of heat flux to simulate the residual stress in a bridge-shaped part built using the PBF process. When a fraction of a layer was activated, its initial temperature was set as the melting temperature of the material. For computational efficiency, they used sequentially coupled thermomechanical analyses. The predicted distortion of the bridge shaped part was within 5% of the experimental measurements. Similarly, Pant et al. [153] analyzed L-shaped samples manufactured using a laser PBF process. They applied a temperature close to the melting point of the material as the initial temperature of the complete layer when it was activated. For validation, the predicted results were compared with the neutron diffraction measurements. Although the predicted stress levels were higher than the measured values, the distribution trends were in good agreement. Prabhakar et al. [167] analyzed tensile test coupons manufactured using an electron beam melting process. Very high temperatures (approx. 1000 °C) were observed in the powder bed, base plate, and build in the electron beam melting process. A uniform temperature close to the melting point of the material was applied to a complete layer to analyze the building process. The temperature was controlled using a profile curve such that, after cooling, the layer temperature became equal to the temperature of the powder bed. A sequentially coupled thermomechanical analysis was adopted for computational efficiency. The simulation results are qualitatively comparable to the deformations observed in the build. Psihoyos et al. [168] analyzed two different parts manufactured using a laser PBF process. They applied a uniform temperature close to the melting point of the material to the complete layer when it was activated. The predicted results captured the general trends of residual strain and stress; however, in some regions, there were discrepancies. Bresson et al. [169] simulated a part using a cone-shaped support. Upon the activation of the layer, the initial temperature was set to the melting temperature of the material. Brick elements were used to mesh the part and supports; however, these elements could not represent the region connecting the supports to the part, owing to the narrowing of the support. Alternatively, supports have been developed using 1D-beam elements. A uniformly reduced cross-section was specified for the beam elements to model narrowing. Physical tests revealed that the mechanical properties of the supports were significantly different from those of the bulk materials. This was attributed to the different thermal histories of the supports. A ductile damage initiation criterion was specified for the beam elements to model the breakage of supports. The simulation was able to predict the detachment of supports from the part, but the predicted number of detached supports was higher than the number of detached supports during the building process.

3.2.1. Final comments

The predictions obtained using simplified models are considered less accurate than those obtained using high-fidelity models owing to the simplifications introduced in such models. The most recent efforts [124,161] to refine the inherent strain approach appear to hold promise for increasing the accuracy while maintaining a low computational expense. The flash heating method requires more computational resources than the inherent strain method but typically provides more accurate predictions. This is attributed to the fact that the flash heating method can at least partially account for the nonuniform temperature history experienced by different regions of a part and because a temperature-dependent elastoplastic material model was used throughout the analysis [50]. The main advantage of high-fidelity models is that they can simulate part-building processes according to the actual scanning strategies. However, the effects of the scanning strategy cannot be captured when agglomeration techniques are used [98]. Therefore, the flash heating

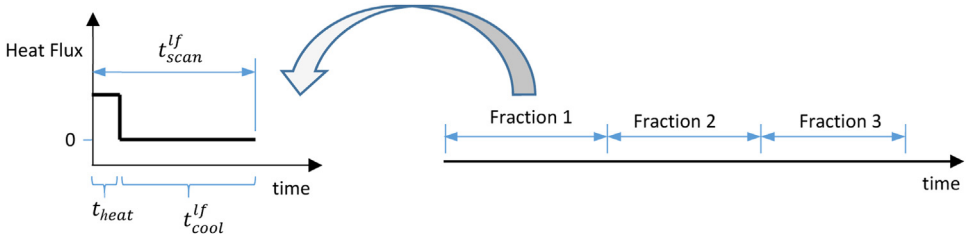

(a) Time decomposition of a single fraction (b) Successive processing of fractions of a layer

Fig. 23. Treatment of layer fractions [151].

method is generally more attractive because it is considerably cheaper than high-fidelity methods.

4. Data-driven Methods in AM Simulation

Mechanistic models (e.g., finite element models) can predict part attributes, such as temperature, distortion, and microstructure, using information about process variables. If data are available on process variables and product attributes, data-driven methods can help understand the relationship between them. Once the relationship is established, predictions can be made regarding the part attributes without using computationally expensive mechanistic models. Predictions made using data-driven tools are very rapid compared to those made using mechanistic models. The accuracy of the predictions improves with an increase in the volume of available data. Data from real-world experiments and previously run simulations were collected and analyzed to gain a better understanding of how different factors affect the quality and performance of AM-produced parts [170]. As the accuracy of predictions made by data-driven methods improves, the need for trial-and-error methodologies and simulations to optimize the AM process is reduced. Thus, data-driven models help save costs and time and improve the quality of parts produced by AM [171].

Machine learning, a subset of artificial intelligence, allows a machine or system to learn from data and make predictions without being explicitly programmed [172]. Machine learning algorithms build a model based on the available data, which is then used to make predictions or decisions. It can quickly recognize data patterns from available data and establish data-driven predictive models [171]. In recent years, machine learning has gained widespread attention in AM owing to its excellent performance in data tasks [172].

Mechanistic models and machine learning, when combined with the knowledge domain of metallurgy, can efficiently and economically provide a link between process variables, component geometry, mechanical properties, microstructure, and defects [47]. Such correlations are important because they help achieve high-quality parts without trial and error.

Data collected from AM processes have been analyzed by different researchers using techniques such as physics-informed neural networks (PINN), quadratic regression (QR), and Gaussian process regression (GPR) [173–175]. Zhu et al. [176] used machine learning techniques to estimate geometric deviation patterns by statistical learning from multiple-shape data. Francis and Bian [177] used a deep learning technique to predict distortion. Thermal images were recorded and analyzed using the algorithm along with the relevant process parameters. The point-wise distortion was measured by scanning after the part was removed from the build plate. The distortion was correlated with the thermal images and process parameters. Analysis of thermal images requires large amounts of memory and significant computational resources. Hence, 26 days were required to train the algorithm. Dong et al. [178] developed a surrogate model to predict the residual stress of parts fabricated using a laser-PBF process. A 3D U-Net convolutional neural network (CNN) was used to build a surrogate model. A high-fidelity model was used to analyze the part geometry and generate training data. The results indicated that the CNN model could accurately predict the stress field. Li et al. [179] used a data-driven approach to predict the layer-by-layer thermal history of a laser PBF-built part. Results of finite element analysis were sampled to establish a surrogate model based on the functional Gaussian process. Cross-validation showed that the model could accurately predict the thermal field for different process parameters and geometries.

Machine learning is an effective method to perform intricate pattern recognition and regression analysis without explicitly solving mechanistic models [180]. It can assist engineers in planning, reducing defects, achieving superior microstructures, assessing product quality, and control [172]. The current state of machine learning techniques focusing on AM is covered in state-of-the-art reviews [172,180–183].

5. Measurement of Residual Stresses and Distortion

The validation of a numerical approach to ensure that predictions are accurate is an important consideration in any study. Such validation requires various types of in situ and ex situ measurements. As in-situ monitoring occurs during the building process, it is more challenging than ex-situ measurements [184,185]. Consequently, it is more common to validate an FE model using ex situ measurements [186].

Both destructive and nondestructive techniques are used to measure the residual stress and strain in AM parts. Many of these techniques have already been used for residual stress measurements in welded structures [187,188]. The Vickers microindentation method is considered a simple and fast method for evaluating the residual stress. The two most common destructive measurement techniques are hole drilling and contour methods. The hole-drilling method is a semi-destructive method for evaluating residual stress. This involves the introduction of a small hole into the stressed body. Owing to the drilling of the hole, the stresses are relieved, which leads to a change in the surrounding strain field. This can be quantified and correlated with the relaxed stress. The damage caused to the specimen is localized and, in some cases, can be tolerated or repaired. The hole-drilling method can measure the residual stresses only near the material surface. The contour method is used to measure the stresses deep inside a part [189,190]. Residual stresses remain inside a part when it has reached static equilibrium; therefore, across any section plane, the sum of stresses normal to the plane must be zero [24]. This principle forms the basis of the contouring method. When a part with residual stresses is sectioned to maintain a static equilibrium, the newly cut surfaces deform to relax the stresses such that the net normal stress at the surface is zero. The deformation of the surface was measured and used to estimate the original state of stress in the component by performing a FE analysis. Thus, the contour method can be used to determine the strain distribution on the entire sectioned plane. Practically, the contour method involves cutting a part into two halves, usually using wire EDM, and measuring the surface deformation maps or contours on the free surfaces created by the cut. The deformations of the cut surface were measured using a coordinate measurement machine, a laser scanner, or digital image correlation. A deformation map was used to compute the residual stresses by performing a finite element

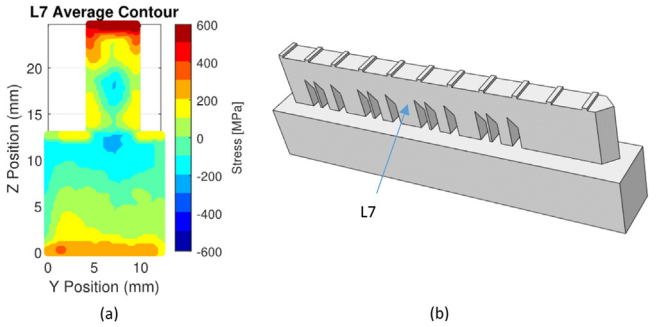

Fig. 24. (a) Contour plot of longitudinal residual stresses using the contour method through 7th leg (L7) (Courtesy www.hill-engineering.com) [191]; (b) Measurement location for the residual stress in the bridge.

analysis [191]. The result of the analysis is a 2-D map of the residual stress normal to the measurement plane.

In Refs. [192,193], residual stress measurements in AM parts were performed using Vickers microindentation. In Refs. [194,195], residual stress measurements in AM parts were performed using the hole drilling method. In Ref. [191], the contour method was used to measure residual stresses in bridge-shaped parts. After the wire EDM operation, the two cut surface profiles were measured, and the forms of each half of the cut surface pair were averaged to eliminate the effects of shear stress and cut path variation. The negative value of the average surface form was used as a displacement boundary condition in the linear elastic stress analysis to estimate the residual stress as a function of the position on the cut plane. The bridge was not symmetrical; therefore, two separate stress analyses were performed, each using the geometry of half of the cut part. The final measured stress was assumed to be the average of the two stress analyses (Fig. 24). In Ref. [196], the contour method was used to measure residual stresses in a cantilever beam. The measurement results were compared with those of numerical simulations. A good correlation was observed between the numerical predictions and the contour method.

The two most commonly used nondestructive methods for measuring residual strains are X-ray diffraction [197] and neutron diffraction [198,199]. These methods exploit the fact that, when a metal is under stress, the resulting elastic strain causes atomic planes in the crystal structure to change their spacing [187]. Diffraction analysis techniques involve determination of the crystallographic structure of a material by irradiation. Radiation is diffracted by atomic planes in the crystal. The diffraction patterns provide information on the structure of the material. By measuring the intensities and scattering angles of the radiation leaving the material, changes in the atomic lattice spacing can be detected. The relative changes in the lattice spacing were calibrated using a stress-free material sample. Using this information, the residual strain in the material can be determined. Diffraction techniques can be used to build full-field strain maps by measuring the diffraction spectra at several positions on a plane [24,191]. A contour plot of the residual strain distribution along the longitudinal direction measured using X-ray diffraction for a bridge structure fabricated using the PBF process is shown in Fig. 16.

One advantage of neutron diffraction is its greater penetration depth compared to X-ray diffraction [188]. It allows to measure residual strains at near-surface depths of 0.2 mm, down to a bulk measurement of up to a few centimeters deep into material [187]. However, the neutron diffraction technique does not offer as good a spatial resolution as X-ray diffraction. Therefore, part characteristics such as fatigue, which may depend on residual stresses or strains close to the surface, might be better investigated using the X-ray diffraction technique [191]. Another advantage of neutron diffraction is that it provides all three orthogonal strain components, whereas X-ray diffraction can only provide two orthogonal components [187,191]. This is because the X-ray diffraction

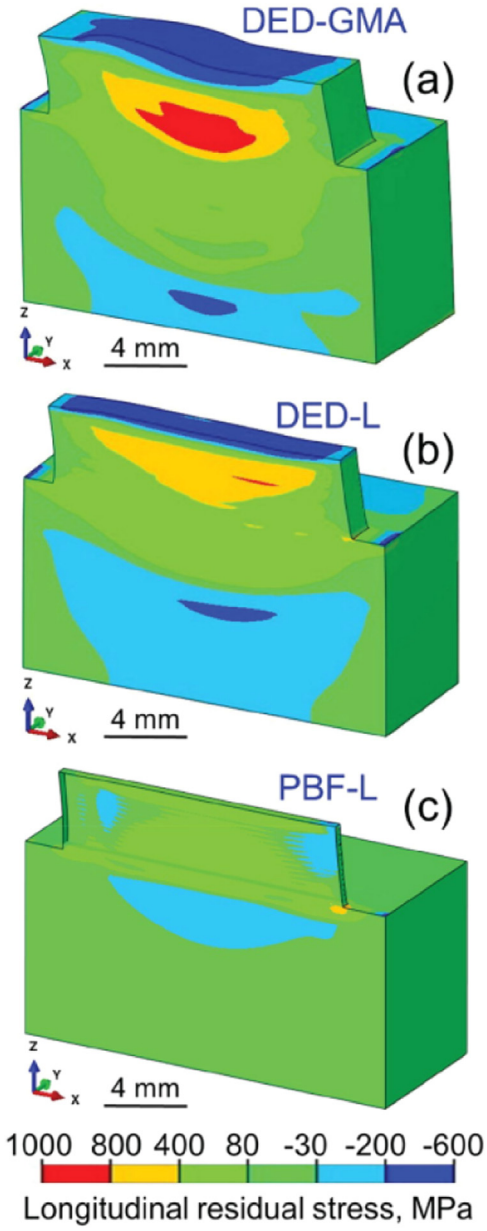

Fig. 25. Contour plot of computed longitudinal residual stress using (a) DED-GMA (b) DED-L and (c) PBF-L process; Each part is 16 mm long, 4 mm high and fabricated on a 20 mm long, 10 mm wide and 10 mm thick substrate; The parts are fabricated using 4, 5 and 16 layers respectively as each process has different characteristic layer thicknesses [213].

technique has limits in measuring the thickness of a structure [187]. Because of the missing strain component, it is not possible to compute the stresses unless a simplifying assumption such as plane stress is introduced [188]. The choice of the measurement technique depends on the part size, material, and spatial resolution requirements [191]. Table 1 summarizes the capabilities of these measurement techniques.

Ganeriwala et al. [50] simulated the strain field in an AM-built part and compared it with synchrotron X-ray diffraction measurements. Wu et al. [200] used X-ray diffraction measurements to validate the predicted numerical results of stress analysis in a part fabricated using the selective laser melting process. Good qualitative and quantitative agreements were observed. Phan et al. [191] measured the residual strain in a PBF-built part using X-ray and neutron diffraction techniques. The comparisons revealed a high degree of agreement between X-ray and neu-

Table 1
Summary of the capabilities of measurement techniques according to Ref. [191].

Technique	Spatial resolution	Penetration	Complete strain/stress state
Neutron diffraction	10^{-3}	High	Yes
X-ray diffraction	10^{-4}	Medium	No

tron diffraction results. However, neutron diffraction was unable to capture the large strain gradients near the edges of the part. The higher effective spatial resolution of X-ray diffraction allowed the measurements to be much closer to the edges of the part. Labudovic and Kovacevic [201] developed a numerical model for simulating the residual stresses in parts fabricated using the direct laser metal powder deposition process. They compared the numerical results with X-ray measurements and found good agreement. Takase et al. [202] used high-precision X-ray diffraction to investigate the influence of the manufacturing method on the distribution of residual stress and phase evolution. The investigation helped correlate the different phase structures with the cooling rates. An et al. [203] used neutron diffraction to measure the strain distribution in an Inconel 625 part fabricated via PBF. Jayanath and Achuthan [204] measured the residual elastic strain via neutron diffraction in a thin-walled part fabricated using DED. Wu et al. [205] used a digital image correlation-based method in conjunction with sectioning to measure surface-level residual stresses. They compared these results with those of neutron diffraction measurements and observed good agreement. Rangaswamy et al. [190] measured the residual stresses in parts fabricated via DED using the neutron diffraction method. They compared the results with stresses measured using the contour method and reported good agreement. Pant et al. [153] developed a simplified model to predict the residual stresses in parts manufactured using the laser PBF method and validated it using the results from neutron diffraction measurements.

In-situ measurements can be performed to measure or infer the residual stresses and distortions during fabrication. Several researchers have used laser displacement sensors to measure substrate distortion during part fabrication using the DED process [68,102,129,135,206]. This provided additional information that would remain uncaptured if only ex situ measurements were used. Temperature history is one of the most commonly used variables to validate numerical models. Digital cameras and photodiodes are frequently used as noncontact temperature measurement devices. They measur radiation from an object whose temperature is to be measured. High-speed cameras are commonly used to observe the molten pool size and oscillation [112,194,201,207,208]. Embedded thermocouples have been widely used to measure the temperature on or within a substrate [100,124,209]. They are then placed away from the molten region. The digital image correlation (DIC) technique provides the full-field displacement of a target object by comparing images recorded before and after deformation [210]. The strain field can be computed using the measured displacement [211]. Therefore, a robust numerical differentiation algorithm is required. Furthermore, residual stresses can be inferred from the displacement field measured using DIC [212]. In-situ residual stress measurement faces significant technical challenges and is an emerging field of research [184,185].

6. Miscellaneous

The selection of an AM process for a given component can also be considered from the perspective of the residual stress and strain. Mukherjee and DebRoy [213] investigated the printability of 316 stainless steel for three different AM processes and found that the residual stresses in components built using DED with a gas-metal arc were approximately six times higher than the stresses in components built using PBF with a laser heat source. This is attributed to the deposition of thicker layers during the DED process. Furthermore, the residual stresses in a DED-fabricated part using a laser as a heat source were greater than the stress in a PBF-fabricated part using a laser as a heat source. Fig. 25 shows the distribution of residual stresses for each part fabricated using different processes. Goel et al. [214] manufactured two similar parts of alloy 718 using the PBF process, one with a laser and the other with an electron beam as the energy source. Neutron diffraction measurements showed that the part built using an electron beam had a significantly lower residual stress than the part built using a laser as the energy source. This was attributed to the lower temperature gradient in the former owing to the higher temperature of the build plate [215]. These results agree with those reported by Sochalski-Kolbus et al. [216]. Takase et al. [202] fabricated specimens using laser PBF and electron beam powder processes to investigate the influence of the manufacturing method on the distribution of residual stress and phase evolution. The specimens were analyzed using high-precision X-ray diffraction (XRD). The specimens fabricated using an electron beam exhibited significantly lower residual stresses than those fabricated using a laser beam as the heat source.

Simplified models using techniques such as layer lumping and adaptive meshing make it possible to simulate the residual deformation of components in an industrial environment. It is possible to make such simulations more efficient by making better use of the available hardware resources. Dugast et al. [217] developed an FE model for the FH simulation of a part built using the PBF process. They used a specially developed solver for the analysis to take advantage of parallel computing and matrix-free methods. The matrix-free method

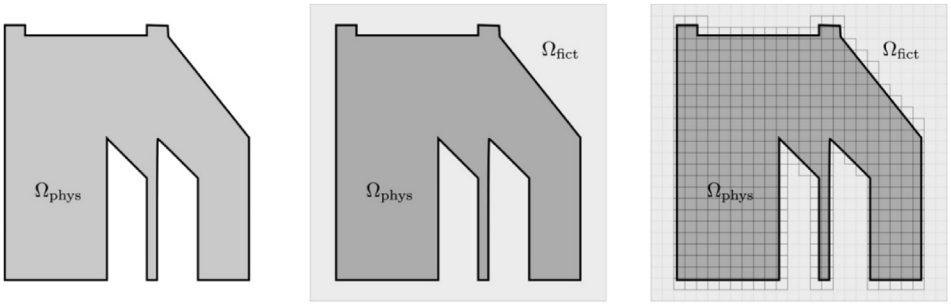

(a) Physical domain Ω_{phys}. (b) Fictitious domain extension. (c) Finite cell mesh.

Fig. 26. Illustration of basic idea the finite cell method [218].

was used to avoid the assembly of the global matrix by performing all matrix-vector products at the element or node level. They reported that the matrix-free solver achieved 1.8 times faster completion than ANSYS APDL while using a single CPU. They also reported that the analysis was 300 times faster when the matrix-free solver was run on a GPU than when it was run on a CPU.

Carraturo et al. [218] employed the finite cell method instead of the finite element method to simulate the residual stress and strain. They used a flash heating method in a finite cell framework. They reported that the analysis was completed in less than 90 min, with a very good correlation with neutron diffraction measurements of the strain distribution. The finite cell method belongs to a class of embedded domain methods, also called fictitious domain or immersed boundary methods [219]. The FE method requires domain discretization that conforms to the physical boundary of the component to be analyzed. For components with complex geometries, such discretization can result in a large number of DoFs. The finite cell method can be an attractive alternative because it allows the use of a significantly coarser mesh because the elements do not need to conform to the boundary of the physical domain. Fig. 26 illustrates the basic concept of the finite-cell method. The physical domain, denoted as Ω_{phys}, represents a generic initial domain. The finite cell method extends the physical domain by adding a fictitious domain, denoted as Ω_{fict}, so that the final domain has a simple geometry that can be trivially discretized using regular elements.

To run simulations faster, Hodge [220] investigated an alternative representation of the temporal evolution of the thermal problem in the PBF process. Two numerical methods are considered: multirate time integration and parallel-in-time integration. These methods have been applied to the two-dimensional heat transfer problem of the PBF process. A speed-up of solution calculations by 40 ~100 times has been reported.

7. Conclusions

A review is presented on the core aspects of residual stress and deformation modeling of parts built using AM processes. The major aspects of the high-fidelity modeling approach are described in detail. One of the important challenges for this approach is the significant computational resources required for accurate analysis. Different techniques used by researchers to make the analysis more efficient have been described previously. Simplified models in which radical assumptions are introduced to estimate a part's behavior faster have been outlined. Two of the most popular simplified approaches are described in detail. Most researchers have validated these approaches by comparing the part-level residual distortions predicted by numerical simulations with those measured by physical tests. However, the validation of the distribution of residual stress and strain is lacking in the literature. The most common measurement techniques used for validating numerical predictions are also reviewed.

Accurate prediction of the residual stress and deformation of a built part using computational models will reduce waste material and time lost owing to failed or out-of-tolerance parts. Several promising models have been developed and used to predict the behavior of AM parts. However, a fully predictive and accurate model that can be used on an industrial scale for various engineering materials is of great interest.

Declaration of Competing Interest

The authors declare that they have no known competing financial interests or personal relationships that may have influenced the work reported in this study.

CRediT authorship contribution statement

Asim Rashid: Conceptualization, Resources, Writing – original draft, Writing – review & editing. **Aditya Gopaluni:** Writing – original draft.

Acknowledgment

Part of this paper was written when the author was employed as researcher at Örebro University, Sweden.

References

[1] Frazier WE. Metal additive manufacturing: a review. J Mater Eng Perform 2014;23:1917–28. doi:10.1007/s11665-014-0958-z.
[2] Collins PC, Brice DA, Samimi P, et al. Microstructural control of additively manufactured metallic materials. Annu Rev Mater Res 2016;46:63–91. doi:10.1146/annurev-matsci-070115-031816.
[3] Lehmann T, Rose D, Ranjbar E, et al. Large-scale metal additive manufacturing: a holistic review of the state of the art and challenges. Int Mater Rev 2022;67:410–59. doi:10.1080/09506608.2021.1971427.
[4] Svetlizky D, Das M, Zheng B, et al. Directed energy deposition (DED) additive manufacturing: physical characteristics, defects, challenges and applications. Mater Today 2021;49:271–95. doi:10.1016/j.mattod.2021.03.020.
[5] Gu DD, Meiners W, Wissenbach K, et al. Laser additive manufacturing of metallic components: materials, processes and mechanisms. Int Mater Rev 2012;57:133–64. doi:10.1179/1743280411Y.0000000014.
[6] Liu J, Gaynor AT, Chen S, et al. Current and future trends in topology optimization for additive manufacturing. Struct Multidiscip Optim 2018;57:2457–83. doi:10.1007/s00158-018-1994-3.
[7] Oropallo W, Piegl LA. Ten challenges in 3D printing. Eng Comput 2016;32:135–48. doi:10.1007/s00366-015-0407-0.
[8] Papadakis L, Loizou A, Risse J, et al. A computational reduction model for appraising structural effects in selective laser melting manufacturing: a methodical model reduction proposed for time-efficient finite element analysis of larger components in selective laser melting. Virtual Phys Prototyp 2014;9:17–25. doi:10.1080/17452759.2013.868005.
[9] Hodge NE, Ferencz RM, Solberg JM. Implementation of a thermomechanical model for the simulation of selective laser melting. Comput Mech 2014;54:33–51. doi:10.1007/s00466-014-1024-2.
[10] Hussein A, Hao L, Yan C, et al. Finite element simulation of the temperature and stress fields in single layers built without-support in selective laser melting. Mater Des 2013;52:638–47. doi:10.1016/j.matdes.2013.05.070.
[11] Mercelis P, Kruth JP. Residual stresses in selective laser sintering and selective laser melting. Rapid Prototyp J 2006;12:254–65. doi:10.1108/13552540610707013.
[12] Rashid A. Overview of disc brakes and related phenomena - a review. Int J Veh Noise Vib 2014;10:257–301. doi:10.1504/IJVNV.2014.065634.
[13] Rashid A, Strömberg N. An efficient sequential approach for simulation of thermal stresses in disc brakes. In: Proceedings of the 15th Nordic Symposium on Tribology NORDTRIB. Norway: Trondheim; 2012.
[14] Fayazfar H, Salarian M, Rogalsky A, et al. A critical review of powder-based additive manufacturing of ferrous alloys: process parameters, microstructure and mechanical properties. Mater Des 2018;144:98–128. doi:10.1016/j.matdes.2018.02.018.
[15] Leuders S, Thöne M, Riemer A, et al. On the mechanical behaviour of titanium alloy TiAl6V4 manufactured by selective laser melting: fatigue resistance and crack growth performance. Int J Fatigue 2013;48:300–7. doi:10.1016/j.ijfatigue.2012.11.011.
[16] Yadollahi A, Shamsaei N. Additive manufacturing of fatigue resistant materials: challenges and opportunities. Int J Fatigue 2017;98:14–31. doi:10.1016/j.ijfatigue.2017.01.001.
[17] Becker TH, Kumar P, Ramamurty U. Fracture and fatigue in additively manufactured metals. Acta Mater 2021;219:117240. doi:10.1016/j.actamat.2021.117240.
[18] Zerbst U, Bruno G, Buffière JY, et al. Damage tolerant design of additively manufactured metallic components subjected to cyclic loading: state of the art and challenges. Prog Mater Sci 2021;121:1–73. doi:10.1016/j.pmatsci.2021.100786.
[19] Wei Q, Xie Y, Teng Q, et al. Crack types, mechanisms, and suppression methods during high-energy beam additive manufacturing of nickel-based superalloys: a review. Chinese J Mech Eng Addit Manuf Front 2022;1:100055. doi:10.1016/j.cjmeam.2022.100055.
[20] Yang G, Xie Y, Zhao S, et al. Quality control: internal defects formation mechanism of selective laser melting based on laser-powder-melt pool interaction: a review. Chin J Mech Eng Addit Manuf Front 2022;1:100037. doi:10.1016/j.cjmeam.2022.100037.
[21] Laleh M, Sadeghi E, Revilla RI, et al. Heat treatment for metal additive manufacturing. Prog Mater Sci 2023;133:101051. doi:10.1016/j.pmatsci.2022.101051.
[22] Li C, Liu JF, Fang XY, et al. Efficient predictive model of part distortion and residual stress in selective laser melting. Addit Manuf 2017;17:157–68. doi:10.1016/j.addma.2017.08.014.
[23] Withers PJ, Bhadeshia HKDH. Residual stress part 1 - Measurement techniques. Mater Sci Technol 2001;17:355–65. doi:10.1179/026708301101509980.
[24] Bartlett JL, Li X. An overview of residual stresses in metal powder bed fusion. Addit Manuf 2019;27:131–49. doi:10.1016/j.addma.2019.02.020.
[25] Rashid A. Finite element modeling of contact problems. Linköping: Linköping University; 2016. doi:103384/dissdiva-124572.
[26] Chen S, Gao H, Zhang Y, et al. Review on residual stresses in metal additive manufacturing: formation mechanisms, parameter dependencies, prediction and control approaches. J Mater Res Technol 2022;17:2950–74. doi:10.1016/j.jmrt.2022.02.054.

[27] Simson T, Emmel A, Dwars A, et al. Residual stress measurements on AISI 316L samples manufactured by selective laser melting. Addit Manuf 2017;17:183–9. doi:10.1016/j.addma.2017.07.007.
[28] Liang X, Cheng L, Chen Q, et al. A modified method for estimating inherent strains from detailed process simulation for fast residual distortion prediction of single-walled structures fabricated by directed energy deposition. Addit Manuf 2018;23:471–86. doi:10.1016/j.addma.2018.08.029.
[29] Liverani E, Toschi S, Ceschini L, et al. Effect of selective laser melting (SLM) process parameters on microstructure and mechanical properties of 316L austenitic stainless steel. J Mater Process Technol 2017;249:255–63. doi:10.1016/j.jmatprotec.2017.05.042.
[30] Wang D, Feng Y, Liu L, et al. Influence mechanism of process parameters on relative density, microstructure, and mechanical properties of low Sc-Content Al-Mg-Sc-Zr alloy fabricated by selective laser melting. Chin J Mech Eng Addit Manuf Front 2022;1:100034. doi:10.1016/j.cjmeam.2022.100034.
[31] Zhang K, Wang S, Liu W, et al. Characterization of stainless steel parts by laser metal deposition shaping. Mater Des 2014;55:104–19. doi:10.1016/j.matdes.2013.09.006.
[32] Liu J, Song Y, Chen C, et al. Effect of scanning speed on the microstructure and mechanical behavior of 316L stainless steel fabricated by selective laser melting. Mater Des 2020;186:108355. doi:10.1016/j.matdes.2019.108355.
[33] Mukherjee T, Manvatkar V, De A, et al. Mitigation of thermal distortion during additive manufacturing. Scr Mater 2017;127:79–83. doi:10.1016/j.scriptamat.2016.09.001.
[34] Liu Y, Yang Y, Wang D. A study on the residual stress during selective laser melting (SLM) of metallic powder. Int J Adv Manuf Technol 2016;87:647–56. doi:10.1007/s00170-016-8466-y.
[35] Song J, Zhang L, Wu W, et al. Understanding processing parameters affecting residual stress in selective laser melting of Inconel 718 through numerical modeling. J Mater Res 2019;34:1395–404. doi:10.1557/jmr.2018.504.
[36] Shiomi M, Osakada K, Nakamura K, et al. Residual stress within metallic model made by selective laser melting process. CIRP Ann - Manuf Technol 2004;53:195–8. doi:10.1016/S0007-8506(07)60677-5.
[37] Xiao Z, Chen C, Zhu H, et al. Study of residual stress in selective laser melting of Ti6Al4V. Mater Des 2020;193:108846. doi:10.1016/j.matdes.2020.108846.
[38] Kruth JP, Deckers J, Yasa E, et al. Assessing influencing factors of residual stresses in SLM using a novel analysis method. In: 16th Int Symp Electromachining. ISEM; 2010. p. 531–7.
[39] Robinson JH, Ashton IRT, Jones E, et al. The effect of hatch angle rotation on parts manufactured using selective laser melting. Rapid Prototyp J 2019;25:289–98. doi:10.1108/RPJ-06-2017-0111.
[40] Strantza M, Ganeriwala RK, Clausen B, et al. Effect of the scanning strategy on the formation of residual stresses in additively manufactured Ti-6Al-4V. Addit Manuf 2021;45:102003. doi:10.1016/j.addma.2021.102003.
[41] Nadammal N, Mishurova T, Fritsch T, et al. Critical role of scan strategies on the development of microstructure, texture, and residual stresses during laser powder bed fusion additive manufacturing. Addit Manuf 2021;38:101792. doi:10.1016/j.addma.2020.101792.
[42] Zhang J, Wang X, Paddea S, et al. Fatigue crack propagation behaviour in wire + arc additive manufactured Ti-6Al-4V: effects of microstructure and residual stress. Mater Des 2016;90:551–61. doi:10.1016/j.matdes.2015.10.141.
[43] Sarkar S, Kumar CS, Nath AK. Effect of different heat treatments on mechanical properties of laser sintered additive manufactured parts. J Manuf Sci Eng Trans ASME 2017;139:111010. doi:10.1115/1.4037437.
[44] Molaei R, Fatemi A, Phan N. Significance of hot isostatic pressing (HIP) on multiaxial deformation and fatigue behaviors of additive manufactured Ti-6Al-4V including build orientation and surface roughness effects. Int J Fatigue 2018;117:352–70. doi:10.1016/j.ijfatigue.2018.07.035.
[45] Bikas H, Stavropoulos P, Chryssolouris G. Additive manufacturing methods and modeling approaches: a critical review. Int J Adv Manuf Technol 2016;83:389–405. doi:10.1007/s00170-015-7576-2.
[46] Megahed M, Mindt HW, N'Dri N, et al. Metal additive-manufacturing process and residual stress modeling. Integr Mater Manuf Innov 2016;5:4. doi:10.1186/s40192-016-0047-2.
[47] DebRoy T, Mukherjee T, Wei HL, et al. Metallurgy, mechanistic models and machine learning in metal printing. Nat Rev Mater 2021;6:48–68. doi:10.1038/s41578-020-00236-1.
[48] Foteinopoulos P, Papacharalampopoulos A, Stavropoulos P. On thermal modeling of additive manufacturing processes. CIRP J Manuf Sci Technol 2018;20:66–83. doi:10.1016/j.cirpj.2017.09.007.
[49] Hodge NE, Ferencz RM, Vignes RM. Experimental comparison of residual stresses for a thermomechanical model for the simulation of selective laser melting. Addit Manuf 2016;12:159–68. doi:10.1016/j.addma.2016.05.011.
[50] Ganeriwala RK, Strantza M, King WE, et al. Evaluation of a thermomechanical model for prediction of residual stress during laser powder bed fusion of Ti-6Al-4V. Addit Manuf 2019;27:489–502. doi:10.1016/j.addma.2019.03.034.
[51] Olleak A, Xi Z. Simulation of layer-by-layer selective laser melting process with an efficient remeshing technique. Procedia Manuf 2019;34:613–18. doi:10.1016/j.promfg.2019.06.167.
[52] Zaeh MF, Branner G. Investigations on residual stresses and deformations in selective laser melting. Prod Eng 2010;4:35–45. doi:10.1007/s11740-009-0192-y.
[53] Chen Q, Liang X, Hayduke D, et al. An inherent strain based multiscale modeling framework for simulating part-scale residual deformation for direct metal laser sintering. Addit Manuf 2019;28:406–18. doi:10.1016/j.addma.2019.05.021.
[54] King W, Anderson AT, Ferencz RM, et al. Overview of modelling and simulation of metal powder bed fusion process at Lawrence Livermore National Laboratory. Mater Sci Technol (United Kingdom) 2015;31:957–68. doi:10.1179/1743284714Y.0000000728.
[55] Markl M, Körner C. Multiscale modeling of powder bed-based additive manufacturing. Annu Rev Mater Res 2016;46:93–123. doi:10.1146/annurev–matsci-070115-032158.
[56] Meier C, Penny RW, Zou Y, et al. Thermophysical phenomena in metal additive manufacturing by selective laser melting: fundamentals, modeling, simulation, and experimentation. Annu Rev Heat Transf 2018;20:241–316. doi:10.1615/annual-revheattransfer.2018019042.
[57] Luo Z, Zhao Y. A survey of finite element analysis of temperature and thermal stress fields in powder bed fusion additive manufacturing. Addit Manuf 2018;21:318–32. doi:10.1016/j.addma.2018.03.022.
[58] Bertini L, Bucchi F, Frendo F, et al. Residual stress prediction in selective laser melting. Int J Adv Manuf Technol 2019;105:609–36. doi:10.1007/s00170-019-04091-5.
[59] DebRoy T, Wei HL, Zuback JS, et al. Additive manufacturing of metallic components – process, structure and properties. Prog Mater Sci 2018;92:112–224. doi:10.1016/j.pmatsci.2017.10.001.
[60] Wei HL, Mukherjee T, Zhang W, et al. Mechanistic models for additive manufacturing of metallic components. Prog Mater Sci 2021;116:100703. doi:10.1016/j.pmatsci.2020.100703.
[61] Bayat M, Dong W, Thorborg J, et al. A review of multi-scale and multi-physics simulations of metal additive manufacturing processes with focus on modeling strategies. Addit Manuf 2021;47:102278. doi:10.1016/j.addma.2021.102278.
[62] Xie D, Lv F, Yang Y, et al. A review on distortion and residual stress in additive manufacturing. Chin J Mech Eng Addit Manuf Front 2022;1:100039. doi:10.1016/j.cjmeam.2022.100039.
[63] Qin L, Wang K, Li X, et al. Review of the formation mechanisms and control methods of geometrical defects in laser deposition manufacturing. Chin J Mech Eng Addit Manuf Front 2022;1:100052. doi:10.1016/j.cjmeam.2022.100052.
[64] Al Hamahmy MI, Deiab I. Review and analysis of heat source models for additive manufacturing. Int J Adv Manuf Technol 2020;106:1223–38. doi:10.1007/s00170-019-04371-0.
[65] Wen X, Wang C, Gong Y, et al. Microstructure and mechanical properties of FeCoNiCrAlx high-entropy alloys by selective laser melting. Chin J Mech Eng Addit Manuf Front 2023;2:100069. doi:10.1016/j.cjmeam.2023.100069.
[66] Goldak J, Chakravarti A, Bibby M. A new finite element model for welding heat sources. Metall Trans B 1984;15:299–305. doi:10.1007/BF02667333.
[67] Mirkoohi E, Seivers DE, Garmestani H, et al. Heat source modeling in selective laser melting. Materials (Basel) 2019;12:1–18. doi:10.3390/ma12132052.
[68] Yan L, Zhang Y, Liou F. A conceptual design of residual stress reduction with multiple shape laser beams in direct laser deposition. Finite Elem Anal Des 2018;144:30–7. doi:10.1016/j.finel.2018.02.004.
[69] Luo Z, Zhao Y. Numerical simulation of part-level temperature fields during selective laser melting of stainless steel 316L. Int J Adv Manuf Technol 2019;104:1615–35. doi:10.1007/s00170-019-03947-0.
[70] Irwin J, Michaleris P. A line heat input model for additive manufacturing. J Manuf Sci Eng Trans ASME 2016;138:1–9. doi:10.1115/1.4033662.
[71] Wu CS, Wang HG, Zhang YM. A new heat source model for keyhole plasma arc welding in FEM analysis of the temperature profile. Weld J (Miami, Fla) 2006;85:284–91.
[72] Bayat M, Mohanty S, Hattel JH. A systematic investigation of the effects of process parameters on heat and fluid flow and metallurgical conditions during laser-based powder bed fusion of Ti6Al4V alloy. Int J Heat Mass Transf 2019;139:213–30. doi:10.1016/j.ijheatmasstransfer.2019.05.017.
[73] Zhang Z, Huang Y, Rani Kasinathan A, et al. 3-Dimensional heat transfer modeling for laser powder-bed fusion additive manufacturing with volumetric heat sources based on varied thermal conductivity and absorptivity. Opt Laser Technol 2019;109:297–312. doi:10.1016/j.optlastec.2018.08.012.
[74] Lindgren LE. Finite element modeling and simulation of welding part 1: increased complexity. J Therm Stress 2001;24:141–92. doi:10.1080/01495730150500442.
[75] Joshi S, Hildebrand J, Aloraier AS, et al. Characterization of material properties and heat source parameters in welding simulation of two overlapping beads on a substrate plate. Comput Mater Sci 2013;69:559–65. doi:10.1016/j.commatsci.2012.11.029.
[76] Fu G, Gu J, Lourenco MI, et al. Parameter determination of double-ellipsoidal heat source model and its application in the multi-pass welding process. Ships Offshore Struct 2015;10:204–17. doi:10.1080/17445302.2014.937059.
[77] Luo Z, Zhao Y. A survey of finite element analysis of temperature and thermal stress fields in powder bed fusion Additive Manufacturing. Addit Manuf 2018;21:318–32. doi:10.1016/j.addma.2018.03.022.
[78] Mishra AK, Aggarwal A, Kumar A, et al. Identification of a suitable volumetric heat source for modelling of selective laser melting of Ti6Al4V powder using numerical and experimental validation approach. Int J Adv Manuf Technol 2018;99:2257–70. doi:10.1007/s00170-018-2631-4.
[79] Zäh MF, Lutzmann S. Modelling and simulation of electron beam melting. Prod Eng 2010;4:15–23. doi:10.1007/s11740-009-0197-6.
[80] Tran HC, Lo YL. Heat transfer simulations of selective laser melting process based on volumetric heat source with powder size consideration. J Mater Process Technol 2018;255:411–25. doi:10.1016/j.jmatprotec.2017.12.024.
[81] Foroozmehr A, Badrossamay M, Foroozmehr E, et al. Finite element simulation of selective laser melting process considering optical penetration depth of laser in powder bed. Mater Des 2016;89:255–63. doi:10.1016/j.matdes.2015.10.002.
[82] Galati M, Iuliano L, Salmi A, et al. Modelling energy source and powder properties for the development of a thermal FE model of the EBM additive manufacturing process. Addit Manuf 2017;14:49–59. doi:10.1016/j.addma.2017.01.001.

[83] Yue M, Li M, An N, et al. Modeling SEBM process of tantalum lattices. Rapid Prototyp J 2023;29:232–45. doi:10.1108/RPJ-05-2022-0152.
[84] Ye R, Smugeresky JE, Zheng B, et al. Numerical modeling of the thermal behavior during the LENS® process. Mater Sci Eng A 2006;428:47–53. doi:10.1016/j.msea.2006.04.079.
[85] Marimuthu S, Clark D, Allen J, et al. Finite element modelling of substrate thermal distortion in direct laser additive manufacture of an aero-engine component. Proc Inst Mech Eng Part C J Mech Eng Sci 2013;227:1987–99. doi:10.1177/0954406212470363.
[86] Wang L, Felicelli S, Gooroochurn Y, et al. Optimization of the LENS® process for steady molten pool size. Mater Sci Eng A 2008;474:148–56. doi:10.1016/j.msea.2007.04.119.
[87] Zhang Y, Yu G, He X. Numerical study of thermal history in laser aided direct metal deposition process. Sci China Phys Mech Astron 2012;55:1431–8. doi:10.1007/s11433-012-4793-7.
[88] Yang Q, Zhang P, Cheng L, et al. Finite element modeling and validation of thermomechanical behavior of Ti-6Al-4V in directed energy deposition additive manufacturing. Addit Manuf 2016;12:169–77. doi:10.1016/j.addma.2016.06.012.
[89] Ding D, Zhang S, Lu Q, et al. The well-distributed volumetric heat source model for numerical simulation of wire arc additive manufacturing process. Mater Today Commun 2021;27:102430. doi:10.1016/j.mtcomm.2021.102430.
[90] Giarollo DF, Mazzaferro CCP, Mazzaferro JAE. Comparison between two heat source models for wire-arc additive manufacturing using GMAW process. J Braz Soc Mech Sci Eng 2022;44:1–13. doi:10.1007/s40430-021-03307-8.
[91] Martukanitz R, Michaleris P, Palmer T, et al. Toward an integrated computational system for describing the additive manufacturing process for metallic materials. Addit Manuf 2014;1:52–63. doi:10.1016/j.addma.2014.09.002.
[92] Denlinger ER, Irwin J, Michaleris P. Thermomechanical modeling of additive manufacturing large parts. J Manuf Sci Eng Trans ASME 2014;136:1–8. doi:10.1115/1.4028669.
[93] Francois MM, Sun A, King WE, et al. Modeling of additive manufacturing processes for metals: challenges and opportunities. Curr Opin Solid State Mater Sci 2017;21:198–206. doi:10.1016/j.cossms.2016.12.001.
[94] Bugatti M, Semeraro Q. Limitations of the inherent strain method in simulating powder bed fusion processes. Addit Manuf 2018;23:329–46. doi:10.1016/j.addma.2018.05.041.
[95] Michaleris P. Modeling metal deposition in heat transfer analyses of additive manufacturing processes. Finite Elem Anal Des 2014;86:51–60. doi:10.1016/j.finel.2014.04.003.
[96] Uriondo A, Esperon-Miguez M, Perinpanayagam S. The present and future of additive manufacturing in the aerospace sector: a review of important aspects. Proc Inst Mech Eng Part G J Aerosp Eng 2015;229:2132–47. doi:10.1177/0954410014568797.
[97] Yang Y, Allen M, London T, et al. Residual strain predictions for a powder bed fusion inconel 625 single cantilever part. Integr Mater Manuf Innov 2019;8:294–304. doi:10.1007/s40192-019-00144-5.
[98] Ganeriwala RK, Hodge NE, Solberg JM. Towards improved speed and accuracy of laser powder bed fusion simulations via multiscale spatial representations. Comput Mater Sci 2021;187:110112. doi:10.1016/j.commatsci.2020.110112.
[99] Strantza M, Ganeriwala RK, Clausen B, et al. Coupled experimental and computational study of residual stresses in additively manufactured Ti-6Al-4V components. Mater Lett 2018;231:221–4. doi:10.1016/j.matlet.2018.07.141.
[100] Williams RJ, Davies CM, Hooper PA. A pragmatic part scale model for residual stress and distortion prediction in powder bed fusion. Addit Manuf 2018;22:416–25. doi:10.1016/j.addma.2018.05.038.
[101] Cheng B, Shrestha S, Chou K. Stress and deformation evaluations of scanning strategy effect in selective laser melting. Addit Manuf 2016;12:240–51. doi:10.1016/j.addma.2016.05.007.
[102] Denlinger ER, Michaleris P. Effect of stress relaxation on distortion in additive manufacturing process modeling. Addit Manuf 2016;12:51–9. doi:10.1016/j.addma.2016.06.011.
[103] Yan W, Yue Z, Zhang J. Study on the residual stress and warping of stiffened panel produced by electron beam freeform fabrication. Mater Des 2016;89:1205–12. doi:10.1016/j.matdes.2015.10.094.
[104] Riedlbauer D, Steinmann P, Mergheim J. Thermomechanical finite element simulations of selective electron beam melting processes: performance considerations. Comput Mech 2014;54:109–22. doi:10.1007/s00466-014-1026-0.
[105] Schoinochoritis B, Chantzis D, Salonitis K. Simulation of metallic powder bed additive manufacturing processes with the finite element method: a critical review. Proc Inst Mech Eng Part B J Eng Manuf 2017;231:96–117. doi:10.1177/0954405414567522.
[106] Patil N, Pal D, Rafi HK, et al. A generalized feed forward dynamic adaptive mesh refinement and derefinement finite element framework for metal laser sintering - Part I: formulation and algorithm development. J Manuf Sci Eng Trans ASME 2015;137:041001. doi:10.1115/1.4030059.
[107] Gouge M, Denlinger E, Irwin J, et al. Experimental validation of thermomechanical part-scale modeling for laser powder bed fusion processes. Addit Manuf 2019;29:100771. doi:10.1016/j.addma.2019.06.022.
[108] Proell SD, Wall WA, Meier C. A simple yet consistent constitutive law and mortar-based layer coupling schemes for thermomechanical macroscale simulations of metal additive manufacturing processes. Adv Model Simul Eng Sci 2021;8:24. doi:10.1186/s40323-021-00209-1.
[109] Meier C, Fuchs SL, Much N, et al. Physics-based modeling and predictive simulation of powder bed fusion additive manufacturing across length scales. GAMM Mitteilungen 2021;44:1–26. doi:10.1002/gamm.202100014.
[110] Proell SD, Wall WA, Meier C. On phase change and latent heat models in metal additive manufacturing process simulation. Adv Model Simul Eng Sci 2020;7:24. doi:10.1186/s40323-020-00158-1.
[111] Hu H, Argyropoulos SA. Mathematical modelling of solidification and melting: a review. Model Simul Mater Sci Eng 1996;4:371–96. doi:10.1088/0965-0393/4/4/004.
[112] Cheng B, Price S, Lydon J, et al. On process temperature in powder-bed electron beam additive manufacturing: model development and validation. J Manuf Sci Eng Trans ASME 2014;136:1–12. doi:10.1115/1.4028484.
[113] Parry L, Ashcroft IA, Wildman RD. Understanding the effect of laser scan strategy on residual stress in selective laser melting through thermo-mechanical simulation. Addit Manuf 2016;12:1–15. doi:10.1016/j.addma.2016.05.014.
[114] Jeong SH, Park EG, Kang JW, et al. Thermal analysis for simulation of metal additive manufacturing process considering temperature- and history-dependent material properties. Int J Aeronaut Sp Sci 2021;22:52–63. doi:10.1007/s42405-020-00283-6.
[115] Lindgren LE. Finite element modeling and simulation of welding. part 2: improved material modeling. J Therm Stress 2001;24:195–231. doi:10.1080/014957301300006380.
[116] Alberg H, Berglund D. Comparison of plastic, viscoplastic, and creep models when modelling welding and stress relief heat treatment. Comput Methods Appl Mech Eng 2003;192:5189–208. doi:10.1016/j.cma.2003.07.010.
[117] Dai H, Francis JA, Stone HJ, et al. Characterizing phase transformations and their effects on ferritic weld residual stresses with X-rays and neutrons. Metall Mater Trans A Phys Metall Mater Sci 2008;39:3070–8. doi:10.1007/s11661-008-9616-0.
[118] Schilp J, Seidel C, Krauss H, et al. Investigations on temperature fields during laser beam melting by means of process monitoring and multiscale process modelling. Adv Mech Eng 2014;6:217584. doi:10.1155/2014/217584.
[119] Armstrong RW, Walley SM. High strain rate properties of metals and alloys. Int Mater Rev 2008;53:105–28. doi:10.1179/174328008X277795.
[120] Goldak J, Zhou J, Breiguine V, et al. Thermal stress analysis of welds: from melting point to room temperature. Trans JWRI 1996;25(2):185–9.
[121] Hocine S, Van Swygenhoven H, Van Petegem S. Verification of selective laser melting heat source models with operando X-ray diffraction data. Addit Manuf 2021;37:101747. doi:10.1016/j.addma.2020.101747.
[122] Promoppatum P, Rollett AD. Physics-based and phenomenological plasticity models for thermomechanical simulation in laser powder bed fusion additive manufacturing : a comprehensive numerical comparison. Mater Des 2021;204:109658. doi:10.1016/j.matdes.2021.109658.
[123] Wedberg D. Dislocation density based material model applied in FE-simulation of metal cuttings. Luleå: Universitetstryckeriet, Luleå; 2010 http://www.diva-portal.org/smash/get/diva2:999440/FULLTEXT01.pdf.
[124] Dong W, Liang X, Chen Q, et al. A new procedure for implementing the modified inherent strain method with improved accuracy in predicting both residual stress and deformation for laser powder bed fusion. Addit Manuf 2021;47:102345. doi:10.1016/j.addma.2021.102345.
[125] Song X, Feih S, Zhai W, et al. Advances in additive manufacturing process simulation: residual stresses and distortion predictions in complex metallic components. Mater Des 2020;193:108779. doi:10.1016/j.matdes.2020.108779.
[126] Zang W, Gunnars J, Dong P, et al. Improvement and validation of weld residual stress modelling procedure, Sweden: Swedish Radiation Safety Authority; 2009. Stockholm.
[127] Qiao D, Feng Z, Zhang W, et al. Modeling of weld residual plastic strain and stress in dissimilar metal butt weld in nuclear reactors. In: Proceedings of the ASME pressure vessels and piping conference. Volume 6B: materials and fabrication, Paris, France; 2013. July 14–18. doi:10.1115/PVP2013-98081.
[128] Denlinger ER, Heigel JC, Michaleris P. Residual stress and distortion modeling of electron beam direct manufacturing Ti-6Al-4V. Proc Inst Mech Eng Part B J Eng Manuf 2015;229:1803–13. doi:10.1177/0954405414539494.
[129] Heigel JC, Michaleris P, Reutzel EW. Thermo-mechanical model development and validation of directed energy deposition additive manufacturing of Ti-6Al-4V. Addit Manuf 2015;5:9–19. doi:10.1016/j.addma.2014.10.003.
[130] Lindgren LE, Lundbäck A, Fisk M, et al. Simulation of additive manufacturing using coupled constitutive and microstructure models. Addit Manuf 2016;12:144–58. doi:10.1016/j.addma.2016.05.005.
[131] Urevc J, Koc P, Štok B. Numerical simulation of stress relieving of an austenite stainless steel. Stroj Vestnik. J Mech Eng 2009;55:590–8.
[132] Zhao Y, Sun J, Li J, et al. A comparative study on Johnson-Cook and modified Johnson-Cook constitutive material model to predict the dynamic behavior laser additive manufacturing FeCr alloy. J Alloys Compd 2017;723:179–87. doi:10.1016/j.jallcom.2017.06.251.
[133] Gupta AK, Anirudh VK, Singh SK. Constitutive models to predict flow stress in austenitic stainless Steel 316 at elevated temperatures. Mater Des 2013;43:410–18. doi:10.1016/j.matdes.2012.07.008.
[134] Ali H, Ghadbeigi H, Mumtaz K. Effect of scanning strategies on residual stress and mechanical properties of selective laser melted Ti6Al4V. Mater Sci Eng A 2018;712:175–87. doi:10.1016/j.msea.2017.11.103.
[135] Denlinger ER, Heigel JC, Michaleris P, et al. Effect of inter-layer dwell time on distortion and residual stress in additive manufacturing of titanium and nickel alloys. J Mater Process Technol 2015;215:123–31. doi:10.1016/j.jmatprotec.2014.07.030.
[136] Kruth JP, Froyen L, Van Vaerenbergh J, et al. Selective laser melting of iron-based powder. J Mater Process Technol 2004;149:616–22. doi:10.1016/j.jmatprotec.2003.11.051.

[137] Robinson J, Ashton I, Fox P, et al. Determination of the effect of scan strategy on residual stress in laser powder bed fusion additive manufacturing. Addit Manuf 2018;23:13–24. doi:10.1016/j.addma.2018.07.001.
[138] Kruth JP, Badrossamay M, Yasa E, et al. Part and material properties in selective laser melting of metals. In: 16th Int Symp Electromachining. ISEM; 2010. p. 3–14.
[139] Gushchina MO, Kuzminova YO, Kudryavtsev EA, et al. Effect of scanning strategy on mechanical properties of Ti-6Al-4V alloy manufactured by laser direct energy deposition. J Mater Eng Perform 2022;31:2783–91. doi:10.1007/s11665-021-06407-7.
[140] Yu J, Lin X, Ma L, et al. Influence of laser deposition patterns on part distortion, interior quality and mechanical properties by laser solid forming (LSF). Mater Sci Eng A 2011;528:1094–104. doi:10.1016/j.msea.2010.09.078.
[141] Yan H, Shen L, Wang X, et al. Stress and deformation evaluation of the sub-area scanning effect in direct laser-deposited Ti-6Al-4V. Int J Adv Manuf Technol 2018;97:915–26. doi:10.1007/s00170-018-1983-0.
[142] Saboori A, Piscopo G, Lai M, et al. An investigation on the effect of deposition pattern on the microstructure, mechanical properties and residual stress of 316L produced by directed energy deposition. Mater Sci Eng A 2020;780:139179. doi:10.1016/j.msea.2020.139179.
[143] Wang J, Zhang J, Liu G, et al. Effects of scanning strategies on residual stress and deformation by high-power direct energy deposition: island size and laser jump strategy between islands. J Manuf Process 2022;75:23–40. doi:10.1016/j.jmapro.2021.12.054.
[144] Zhou Z, Shen H, Lin J, et al. Continuous tool-path planning for optimizing thermo-mechanical properties in wire-arc additive manufacturing: an evolutional method. J Manuf Process 2022;83:354–73. doi:10.1016/j.jmapro.2022.09.009.
[145] Aliyev A, Lee KK, Ahn DG. Effects of deposition strategies on thermo-mechanical characteristics of inconel 718 deposited region on AISI 1045 substrate with a cantilever structure by LENS process. J Mech Sci Technol 2022;36:4695–705. doi:10.1007/s12206-022-0830-2.
[146] Chen F, Yan W. High-fidelity modelling of thermal stress for additive manufacturing by linking thermal-fluid and mechanical models. Mater Des 2020;196:109185. doi:10.1016/j.matdes.2020.109185.
[147] Jayanath S, Achuthan A. A computationally efficient hybrid model for simulating the additive manufacturing process of metals. Int J Mech Sci 2019;160:255–69. doi:10.1016/j.ijmecsci.2019.06.007.
[148] Santi A, Bayat M, Hattel JH. Multiphysics modelling of metal based additive manufacturing processes 1 with focus on thermomechanical conditions. J Therm Stress 2023;46:445–63. doi:10.1080/01495739.2023.2195513.
[149] Yuan MG, Ueda Y. Prediction of residual stresses in welded T- and I-joints using inherent strains. J Eng Mater Technol Trans ASME 1996;118:229–34. doi:10.1115/1.2804892.
[150] Zhang L, Michaleris P, Marugabandhu P. Evaluation of applied plastic strain methods for welding distortion prediction. J Manuf Sci Eng Trans ASME 2007;129:1000–10. doi:10.1115/1.2716740.
[151] Zhang Y, Guillemot G, Bernacki M, et al. Macroscopic thermal finite element modeling of additive metal manufacturing by selective laser melting process. Comput Methods Appl Mech Eng 2018;331:514–35. doi:10.1016/j.cma.2017.12.003.
[152] Keller N, Neugebauer F, Xu H, et al. Thermo-mechanical simulation of additive layer manufacturing of titanium aerospace structures. Bremen, Germany: LightMAT; 2013.
[153] Pant P, Sjöström S, Simonsson K, et al. A simplified layer-by-layer model for prediction of residual stress distribution in additively manufactured parts. Metals (Basel) 2021;11:1–23. doi:10.3390/met11060861.
[154] Keller N, Ploshikhin V. New method for fast predictions of residual stress and distortion of AM parts. In: Proceedings of the 25th Annual International Solid Freeform Fabrication Symposium; 2014. p. 1229–37. An Addit Manuf Conf SFF 2014.
[155] Deng D, Murakawa H, Liang W. Numerical simulation of welding distortion in large structures. Comput Methods Appl Mech Eng 2007;196:4613–27. doi:10.1016/j.cma.2007.05.023.
[156] Taufek T, Manurung YHP, Lüder S, et al. Distortion analysis of SLM product of SS316L using inherent strain method. IOP Conf Ser Mater Sci Eng 2020;834:1–14. doi:10.1088/1757-899X/834/1/012011.
[157] Setien I, Chiumenti M, van der Veen S, et al. Empirical methodology to determine inherent strains in additive manufacturing. Comput Math with Appl 2019;78:2282–95. doi:10.1016/j.camwa.2018.05.015.
[158] Chen Y, Xu Y, Hou L, et al. Fast distortion prediction in directed energy deposition using inversely-identified inherent strains. J Eng Des 2023;34:294–312. doi:10.1080/09544828.2023.2193879.
[159] Siewert M, Neugebauer F, Epp J, et al. Validation of mechanical layer equivalent method for simulation of residual stresses in additive manufactured components. Comput Math with Appl 2019;78:2407–16. doi:10.1016/j.camwa.2018.08.016.
[160] AdditiveLab. Simulate metal additive manufacturing. Iterate between multiple manufacturing scenarios fast. Build for success. 2019. https://www.additive-lab.com/.
[161] Dong W, Jimenez XA, To AC. Temperature-dependent modified inherent strain method for predicting residual stress and distortion of Ti6Al4V walls manufactured by wire-arc directed energy deposition. Addit Manuf 2023;62:103386. doi:10.1016/j.addma.2022.103386.
[162] Liang X, Dong W, Hinnebusch S, et al. Inherent strain homogenization for fast residual deformation simulation of thin-walled lattice support structures built by laser powder bed fusion additive manufacturing. Addit Manuf 2020;32:101091. doi:10.1016/j.addma.2020.101091.
[163] Noll I, Bartel T, Menzel A. On the incorporation of a micromechanical material model into the inherent strain method—Application to the modeling of selective laser melting. GAMM Mitteilungen 2021;44:1–25. doi:10.1002/gamm.202100015.
[164] Noll I, Koppka L, Bartel T, et al. A micromechanically motivated multiscale approach for residual distortion in laser powder bed fusion processes. Addit Manuf 2022;60:103277. doi:10.1016/j.addma.2022.103277.
[165] Schill M. A layer-by-layer approach for simulating residual stresses in AM. In: Proceedings of the European LS-DYNA conference, Salzburg, Austria; 2017.
[166] Bayat M, Klingaa CG, Mohanty S, et al. Part-scale thermo-mechanical modelling of distortions in laser powder bed fusion – analysis of the sequential flash heating method with experimental validation. Addit Manuf 2020;36:101508. doi:10.1016/j.addma.2020.101508.
[167] Prabhakar P, Sames WJ, Dehoff R, et al. Computational modeling of residual stress formation during the electron beam melting process for Inconel 718. Addit Manuf 2015;7:83–91. doi:10.1016/j.addma.2015.03.003.
[168] Psihoyos HO, Lampeas GN. Efficient thermomechanical modelling of laser powder bed fusion additive manufacturing process with emphasis on parts residual stress fields. AIMS Mater Sci 2022;9:455–80. doi:10.3934/matersci.2022027.
[169] Bresson Y, Tongne A, Selva P, et al. Numerical modelling of parts distortion and beam supports breakage during selective laser melting (SLM) additive manufacturing. Int J Adv Manuf Technol 2022;119:5727–42. doi:10.1007/s00170-021-08501-5.
[170] Moges T, Ameta G, Witherell P. A review of model inaccuracy and parameter uncertainty in laser powder bed fusion models and simulations. J Manuf Sci Eng Trans ASME 2019;141:1–35. doi:10.1115/1.4042789.
[171] Liu J, Ye J, Silva Izquierdo D, et al. A review of machine learning techniques for process and performance optimization in laser beam powder bed fusion additive manufacturing. J Intell Manuf 2022;34:3249–75. doi:10.1007/s10845-022-02012-0.
[172] Wang C, Tan XP, Tor SB, et al. Machine learning in additive manufacturing: state-of-the-art and perspectives. Addit Manuf 2020;36:101538. doi:10.1016/j.addma.2020.101538.
[173] Zhu Q, Liu Z, Yan J. Machine learning for metal additive manufacturing: predicting temperature and melt pool fluid dynamics using physics-informed neural networks. Comput Mech 2021;67:619–35 2021 672. doi:10.1007/S00466-020-01952-9.
[174] Bhardwaj T, Shukla M, Paul CP, et al. Direct energy deposition - laser additive manufacturing of titanium-molybdenum alloy: parametric studies, microstructure and mechanical properties. J Alloys Compd 2019;787:1238–48. doi:10.1016/J.JALLCOM.2019.02.121.
[175] Tapia G, Elwany AH, Sang H. Prediction of porosity in metal-based additive manufacturing using spatial Gaussian process models. Addit Manuf 2016;12:282–90. doi:10.1016/J.ADDMA.2016.05.009.
[176] Zhu Z, Anwer N, Huang Q, et al. Machine learning in tolerancing for additive manufacturing. CIRP Ann 2018;67:157–60. doi:10.1016/j.cirp.2018.04.119.
[177] Francis J, Bian L. Deep learning for distortion prediction in laser-based additive manufacturing using big data. Manuf Lett 2019;20:10–14. doi:10.1016/j.mfglet.2019.02.001.
[178] Dong G, Wong JC, Lestandi L, et al. A part-scale, feature-based surrogate model for residual stresses in the laser powder bed fusion process. J Mater Process Technol 2022;304:117541. doi:10.1016/J.JMATPROTEC.2022.117541.
[179] Li J, Jin R, Yu HZ. Integration of physically-based and data-driven approaches for thermal field prediction in additive manufacturing. Mater Des 2018;139:473–85. doi:10.1016/j.matdes.2017.11.028.
[180] Qi X, Chen G, Li Y, et al. Applying neural-network-based machine learning to additive manufacturing: current applications, challenges, and future perspectives. Engineering 2019;5:721–9. doi:10.1016/j.eng.2019.04.012.
[181] Qin J, Hu F, Liu Y, et al. Research and application of machine learning for additive manufacturing. Addit Manuf 2022;52:102691. doi:10.1016/j.addma.2022.102691.
[182] Kumar S, Gopi T, Harikeerthana N, et al. Machine learning techniques in additive manufacturing: a state of the art review on design, processes and production control. J Intell Manuf 2023;34:21–55. doi:10.1007/s10845-022-02029-5.
[183] Xames MD, Torsha FK, Sarwar F. A systematic literature review on recent trends of machine learning applications in additive manufacturing. J Intell Manuf 2022;34:2529–55. doi:10.1007/s10845-022-01957-6.
[184] Everton SK, Hirsch M, Stavroulakis PI, et al. Review of in-situ process monitoring and in-situ metrology for metal additive manufacturing. Mater Des 2016;95:431–45. doi:10.1016/j.matdes.2016.01.099.
[185] Schmeiser F, Krohmer E, Schell N, et al. Experimental observation of stress formation during selective laser melting using in situ X-ray diffraction. Addit Manuf 2020;32:101028. doi:10.1016/j.addma.2019.101028.
[186] Dunbar AJ, Denlinger ER, Heigel J, et al. Development of experimental method for in situ distortion and temperature measurements during the laser powder bed fusion additive manufacturing process. Addit Manuf 2016;12:25–30. doi:10.1016/j.addma.2016.04.007.
[187] Rossini NS, Dassisti M, Benyounis KY, et al. Methods of measuring residual stresses in components. Mater Des 2012;35:572–88. doi:10.1016/j.matdes.2011.08.022.
[188] Withers PJ, Turski M, Edwards L, et al. Recent advances in residual stress measurement. Int J Press Vessel Pip 2008;85:118–27. doi:10.1016/j.ijpvp.2007.10.007.
[189] Vrancken B, Cain V, Knutsen R, et al. Residual stress via the contour method in compact tension specimens produced via selective laser melting. Scr Mater 2014;87:29–32. doi:10.1016/j.scriptamat.2014.05.016.
[190] Rangaswamy P, Griffith ML, Prime MB, et al. Residual stresses in LENS® components using neutron diffraction and contour method. Mater Sci Eng A 2005;399:72–83. doi:10.1016/j.msea.2005.02.019.
[191] Phan TQ, Strantza M, Hill MR, et al. Elastic residual strain and stress measurements and corresponding part deflections of 3D additive manufacturing builds of IN625 AM-bench artifacts using neutron diffraction, synchrotron X-

Ray diffraction, and contour method. Integr Mater Manuf Innov 2019;8:318–34. doi:10.1007/s40192-019-00149-0.
[192] Lu Y, Wu S, Gan Y, et al. Study on the microstructure, mechanical property and residual stress of SLM Inconel-718 alloy manufactured by differing island scanning strategy. Opt Laser Technol 2015;75:197–206. doi:10.1016/j.optlastec.2015.07.009.
[193] Liu F, Lin X, Yang G, et al. Microstructure and residual stress of laser rapid formed Inconel 718 nickel-base superalloy. Opt Laser Technol 2011;43:208–13. doi:10.1016/j.optlastec.2010.06.015.
[194] Griffith ML, Schlieriger ME, Harwell LD, et al. Understanding thermal behavior in the LENS process. Mater Des 1999;20:107–13. doi:10.1016/s0261-3069(99)00016-3.
[195] Casavola C, Campanelli SL, Pappalettere C. Preliminary investigation on distribution of residual stress generated by the selective laser melting process. J Strain Anal Eng Des 2009;44:93–104. doi:10.1243/03093247JSA464.
[196] Ahmad B, van der Veen SO, Fitzpatrick ME, et al. Residual stress evaluation in selective-laser-melting additively manufactured titanium (Ti-6Al-4V) and inconel 718 using the contour method and numerical simulation. Addit Manuf 2018;22:571–82. doi:10.1016/j.addma.2018.06.002.
[197] Croft M, Zakharchenko I, Zhong Z, et al. Strain field and scattered intensity profiling with energy dispersive x-ray scattering. J Appl Phys 2002;92:578–86. doi:10.1063/1.1483373.
[198] Wimpory RC, Ohms C, Hofmann M, et al. Statistical analysis of residual stress determinations using neutron diffraction. Int J Press Vessel Pip 2009;86:48–62. doi:10.1016/j.ijpvp.2008.11.003.
[199] Webster GA, Wimpory RC. Non-destructive measurement of residual stress by neutron diffraction. J Mater Process Technol 2001;117:395–9. doi:10.1016/S0924-0136(01)00802-0.
[200] Wu J, Wang L, An X. Numerical analysis of residual stress evolution of AlSi10Mg manufactured by selective laser melting. Optik (Stuttg) 2017;137:65–78. doi:10.1016/j.ijleo.2017.02.060.
[201] Labudovic M, Hu D, Kovacevic R. A three dimensional model for direct laser metal powder deposition and rapid prototyping. J Mater Sci 2003;38:35–49. doi:10.1023/A:1021153513925.
[202] Takase A, Ishimoto T, Morita N, et al. Comparison of phase characteristics and residual stresses in ti-6al-4v alloy manufactured by laser powder bed fusion (L-pbf) and electron beam powder bed fusion (eb-pbf) techniques. Crystals 2021;11. doi:10.3390/cryst11070796.
[203] An K, Yuan L, Dial L, et al. Neutron residual stress measurement and numerical modeling in a curved thin-walled structure by laser powder bed fusion additive manufacturing. Mater Des 2017;135:122–32. doi:10.1016/j.matdes.2017.09.018.
[204] Jayanath S, Achuthan A. A computationally efficient finite element framework to simulate additive manufacturing processes. J Manuf Sci Eng Trans ASME 2018;140. doi:10.1115/1.4039092.
[205] Wu AS, Brown DW, Kumar M, et al. An experimental investigation into additive manufacturing-induced residual stresses in 316L stainless steel. Metall Mater Trans A Phys Metall Mater Sci 2014;45:6260–70. doi:10.1007/s11661-014-2549-x.
[206] Malmelöv A, Lundbäck A, Lindgren LE. History reduction by lumping for time-efficient simulation of additive manufacturing. Metals (Basel) 2020;10. doi:10.3390/met10010058.
[207] Foroozmehr E, Kovacevic R. Effect of path planning on the laser powder deposition process: thermal and structural evaluation. Int J Adv Manuf Technol 2010;51:659–69. doi:10.1007/s00170-010-2659-6.
[208] Mirkoohi E, Ning J, Bocchini P, et al. Thermal modeling of temperature distribution in metal additive manufacturing considering effects of build layers, latent heat, and temperature-sensitivity of material properties. J Manuf Mater Process 2018;2:63. doi:10.3390/jmmp2030063.
[209] Mukherjee T, Zhang W, DebRoy T. An improved prediction of residual stresses and distortion in additive manufacturing. Comput Mater Sci 2017;126:360–72. doi:10.1016/j.commatsci.2016.10.003.
[210] Cunha FG, Santos TG, Xavier J. In situ monitoring of additive manufacturing using digital image correlation: a review. Materials (Basel) 2021;14. doi:10.3390/ma14061511.
[211] Biegler M, Graf B, Rethmeier M. In-situ distortions in LMD additive manufacturing walls can be measured with digital image correlation and predicted using numerical simulations. Addit Manuf 2018;20:101–10. doi:10.1016/j.addma.2017.12.007.
[212] Bartlett JL, Croom BP, Burdick J, et al. Revealing mechanisms of residual stress development in additive manufacturing via digital image correlation. Addit Manuf 2018;22:1–12. doi:10.1016/j.addma.2018.04.025.
[213] Mukherjee T, DebRoy T. Printability of 316 stainless steel. Sci Technol Weld Join 2019;24:412–19. doi:10.1080/13621718.2019.1607061.
[214] Goel S, Neikter M, Capek J, et al. Residual stress determination by neutron diffraction in powder bed fusion-built Alloy 718: influence of process parameters and post-treatment. Mater Des 2020;195:109045. doi:10.1016/j.matdes.2020.109045.
[215] Hosseini E, Popovich VA. A review of mechanical properties of additively manufactured Inconel 718. Addit Manuf 2019;30:100877. doi:10.1016/j.addma.2019.100877.
[216] Sochalski-Kolbus LM, Payzant EA, Cornwell PA, et al. Comparison of residual stresses in Inconel 718 simple parts made by electron beam melting and direct laser metal sintering. Metall Mater Trans A Phys Metall Mater Sci 2015;46:1419–32. doi:10.1007/s11661-014-2722-2.
[217] Dugast F, Apostolou P, Fernandez A, et al. Part-scale thermal process modeling for laser powder bed fusion with matrix-free method and GPU computing. Addit Manuf 2021;37:101732. doi:10.1016/j.addma.2020.101732.
[218] Carraturo M, Jomo J, Kollmannsberger S, et al. Modeling and experimental validation of an immersed thermo-mechanical part-scale analysis for laser powder bed fusion processes. Addit Manuf 2020;36:101498. doi:10.1016/j.addma.2020.101498.
[219] Schillinger D, Ruess M. The finite cell method: a review in the context of higher-order structural analysis of CAD and image-based geometric models. Arch Comput Methods Eng 2015;22:391–455. doi:10.1007/s11831-014-9115-y.
[220] Hodge NE. Towards improved speed and accuracy of laser powder bed fusion simulations via representation of multiple time scales. Addit Manuf 2021;37:101600. doi:10.1016/j.addma.2020.101600.